Stiffness Modeling of a 2-DoF Over-Constrained Planar Parallel Mechanism

Ibrahimcan Görgülü[a], Mehmet Ismet Can Dede[a,*] and Gökhan Kiper[a]

[a]*İzmir Institute of Technology, Türkiye*

ARTICLE INFO

Keywords:
Virtual Joint Method
Over-Constrained Structure
Industrial Robots
Stiffness Modeling
Time-efficient Computation

ABSTRACT

Stiffness model acquisition of over-constrained parallel mechanisms is relatively difficult since they have more than necessary kinematic loops. In this study, a stiffness modeling solution for over-constrained parallel mechanisms is proposed while considering the computational cost efficiency. Three contributions of the paper are: (1) Presenting the stiffness modeling procedure for serially connected closed-loop structures by using the Virtual Joint Method (2) Considering the effect of dynamic auxiliary forces and dynamic external forces on the mobile platform's deflection and achieving a direct solution by using superposition principle (3) A model fitting procedure for modifying the stiffness coefficients to comply with the experimental data. A 2 degrees-of-freedom over-constrained parallel mechanism is investigated as a case study. However, the proposed stiffness model is 6-DoF since compliant deflections occur in any direction. A finite element analysis and an experimental study verify the model's results.

1. Introduction

Linkages with high stiffness are desired in the construction of industrial mechanisms to minimize compliant deflections for maintaining accuracy and precision. Stiff linkages result in bulky structures. In return, the system's inertia, power requirements, and electricity cost increase. On the other hand, low-power actuators limit the acceleration of the mechanism and increase the operation time. A solution is to utilize lightweight linkages and address the compliance problem by incorporating the stiffness characteristics of the mechanism in the control system. This work explores the possibility of using a stiffness model within the control system in real time.

Researchers have focused on three stiffness analysis methods of mechanisms. These are the finite element analysis (FEA), the structural matrix analysis (SMA), and the virtual joint method (VJM). The FEA is the most accurate method due to its higher number of meshes and iterative computation methodology. However, the FEA is computationally intensive and not applicable in a real-time control loop. In addition, each linkage must be re-meshed in every configuration change [1]. The SMA is a faster method with fewer meshes and nodes [2]. A simple beam can be modeled with nodes represented by a 12×12 stiffness matrix. A higher number of nodes and several limbs of a parallel manipulator may result in higher dimensional matrices which are challenging in analytical computations [3, 4].

The VJM locates a single node on each link resulting in a 6×6 stiffness matrix per link. Therefore, it is also called lumped method approach. The stiffness properties are lumped on a 6 degrees-of-freedom (DoF) virtual joint (or virtual spring) [4–9]. The smaller size of local stiffness matrices and fewer variables make the VJM the simplest and the fastest method. It is also easier to obtain an analytic stiffness model. This way, a small force-to-deflection ratio can be computed in one computation step. Both the SMA and the VJM generally adopt coordinate transformations; however, strain energy with Castigliano's theorem is used to avoid these transformations. The loss in the computation accuracy with the VJM and the SMA versus the FEA is about 1%, as reported in [10–12]. The gain in computation efficiency for 1% of accuracy loss is about 99.998% as reported in [10] in which the VJM is used to compute the deflections in 0.5 ms. Similarly, a solution of the SMA is obtained in 10 ms in [13].

Stiffness modeling methods have been well-established for serial manipulators which have a single kinematic chain. On the other hand, parallel manipulators have internal stresses, passive joints, and several closed kinematic loops. These increase the complexity of the problem because the contribution of each limb to the stiffness must be considered simultaneously [4, 14, 15]. In addition, auxiliary wrenches on each link should be distributed throughout the bodies of the manipulator that are solved by iterative computations [3]. Nonetheless, parallel mechanisms are known to possess

Email addresses: ibrahimcangorgulu@iyte.edu.tr (I. Görgülü); candede@iyte.edu.tr (M.I.C. Dede); gokhankiper@iyte.edu.tr (G. Kiper)

ORCID(s): 0000-0002-8271-0414 (I. Görgülü); 0000-0001-6220-6678 (M.I.C. Dede); 0000-0001-8793-724X (G. Kiper)

high positioning accuracy compared to serial mechanisms [16, 17]. Over-constrained parallel mechanisms (OCPM) are usually preferred over simply-constrained parallel mechanisms (SCPM) for their higher stiffness [4, 18, 19]. It is also reported that OCPMs have good repeatability [20]. OCPMs have more joints/links than required, which may increase the number of closed kinematic loops, internal stresses, and the number of joints when compared to SCPMs. Also, the manipulator becomes statically indeterminate, which makes it challenging to compute the distribution of the external load on the links; thus, the compliant deflections.

In [21], Hu and Huang obtained the stiffness model of a 2RPU-UPR (U=universal joint, P=prismatic joint, R=revolute joint) OCPMs. Stiffness analysis for a class of OCPMs with US (S=spherical joint) and UPS limbs is formulated in [22]. Ding et al. [23] analyzed the accuracy of an over-constrained Stewart platform with actuation stiffness. Yang et al. [11, 12] obtained the stiffness model of 2UPR-RPU and 2PUR-PSR OCPMs via strain energy computation by achieving 0.8% and 1.3% accuracy loss compared to the FEA. Cao et al. [24, 25] obtained the stiffness model of OCPMs by using an energy method with less than 3% accuracy loss. Cao et al. [26] extended the approach considering the weights of the links in which the weight of each limb is distributed between the mobile platform frame and the base.

The manipulators in the studies above have serial kinematic structures in their limbs. Differently, Sun et al. [27] acquired the stiffness model of a 2-DoF rotational parallel mechanism in which each limb has a closed-loop kinematic chain considering the external wrenches and link weights. Cammatra [28] included the joint flexibility and pre-loading at joints for the manipulators with closed-loop chains such as parallelograms in their limbs resulting in 3% accuracy loss. Pashkevich et al. [4] derived the stiffness model of the 3-DoF Orthoglide parallel manipulator in which each limb has a single parallelogram. Nonetheless, the case for consecutive connections of closed-loop chains is not investigated. Later, auxiliary forces on each link are considered, and the effect of each force on the mobile platform's compliant deflection is determined via an iterative solution since the interaction between the limbs must be considered [3]. Finally, Klimchik et al. [29] derived the stiffness model of NAVARO II. In [29], the connection method of multiple closed-loop chains is illustrated for an external wrench on the mobile platform via SMA; however, the dimensions of the matrices to be computed were relatively high. The fundamentals of the SMA methodology are given in [13].

In this paper, we focus on the stiffness formulation of a 2-DoF planar OCPM by using the VJM. However, the stiffness model is 6-DoF since the compliance may occur in any direction. The novelty and the contribution of this work to the literature on mechanisms and machine science are explained as follows:

(1) The inspected mechanism contains a serial connection of closed loops at its limbs, namely, the serial connection of two parallelograms. To our knowledge, the VJM is applied for a parallelogram loop connected to a distal link at one node, but a serial connection of two parallelograms in which the connection occurs at two nodes is not studied. This proposed stiffness modeling solution method constructs the basis for the serial connection of closed-loop sub-chains.

(2) In the literature, external wrenches at the mobile platform and auxiliary forces on the links are assumed to be caused by the payload/physical interaction and the weight of the links, respectively. In this study, auxiliary loads due to the acceleration of bodies are considered. In [3], weights of the links are considered which can be extended for the dynamic cases. However, the solution relies on iterative computations to converge an equal deflection of all limbs at the mobile platform frame. Without iteration, there is no way to conclude how the weight of a limb affects the other limbs' deflection. In our proposed method, we construct a stiffness model for each auxiliary frame and compute their deflections. Since the joint space deflections are directly obtained, the deflection of all limbs and mobile platform frame are directly computed. Finally, the superposition principle is adopted to compute the resultant deflection. In addition, deflections caused by gravity generally refer to a static case problem. Our aim is to use the stiffness model in a control loop to enhance the deflection performance caused by non-gravitational acceleration. Hence, developing a computationally efficient model is necessary. We also show how to lump the masses directly on the loading frames. In our case study, 11 moving bodies' masses are lumped on two auxiliary and one mobile platform frame.

(3) A model fitting procedure to comply with the experimental load/deflection tests is introduced. Several unknown correction gain parameters are defined for model fitting, in which their values are determined via an optimization process. These gain parameters are formed so that the configuration and non-configuration-dependent values of the stiffness matrix elements can be captured.

This work aims to acquire a compliance model of OCPMs that is computationally efficient and can be used in a real-time control loop. The application of the proposed methodology is straightforward once the initially required matrices and vectors are defined. The procedure avoids defining a specific stiffness matrix for each link depending on its DoF and constraints. The results of the FEA and the VJM are compared to validate the stiffness model and to evaluate the computation time performance. Finally, the stiffness model parameters are updated via an experimental

procedure. The results indicate a good model fit for the mechanism's stiffness characteristics.

2. Stiffness Modeling via the Virtual Joint Method

This section gives brief information for the stiffness modeling of parallel mechanisms via the VJM as explained in detail in [14] and a glossary given in below. This generic formulation may be adapted to the exceptional cases of the problem at hand. These are highlighted in the case study in Section 3.

Nomenclature

Variables		**Notation**	
θ	Virtual joint variable	M	A scalar M variable
φ	Rotary joint variable	$\bar{M}$	M in column matrix form
d	Distance	$\boldsymbol{M}$	M in matrix Form
l	Link length	$\Delta\bar{M}$	Change in $\bar{M}$
k	Stiffness coefficient		
Column Matrices (CM)		**Matrices**	
$\bar{X}$	Task space position in Cartesian coordinates	$\boldsymbol{J}$	Jacobian
$\bar{F}$	Force and torque components	$\boldsymbol{K}$	Stiffness
$\bar{q}_a$	CM of active joints variables	$\boldsymbol{C}$	Compliance
$\bar{q}_p$	CM of passive joint variables	$\boldsymbol{H}$	Homogeneous Transformation
$\bar{\theta}$	CM of virtual joint variables	$\boldsymbol{R}$	Homogeneous Pure Rotation
$\bar{Q}$	CM of all joint variables	$\boldsymbol{T}$	Homogeneous Pure Translation
Sub-indices indicate the component is belong to or derived with respect to			
i	i$^{\text{th}}$ limb	A	Frame A
p	Passive joint	B	Frame B
a	Active joint	E	Mobile platform frame E
θ	Virtual joint	$Eq.$	Equivalent model
L	Kinematic loop	$Eq(Active)$	Eq. Active Parallelogram
x, y, z	x, y, and z coordinate axes	$Eq(Passive)$	Eq. Passive Parallelogram

In the VJM, compliant deflections are small enough to assume $\Delta\bar{X}_i \approx \boldsymbol{J}_i\Delta\bar{Q}_i$ where $\Delta\bar{X}_i$ is the change in position vector of the inspected frame, $\Delta\bar{Q}_i$ is the change in joint space variables, and $\boldsymbol{J}_i$ is the Jacobian matrix of the i^{th} limb in a parallel manipulator. Bar notations indicate the column matrix format. The compliant deflection, applied load, and passive joint's zero-stiffness-effect for the i^{th} limb are constructed in the following block matrix format:

$$\begin{bmatrix} (\boldsymbol{J}_{\theta i}\boldsymbol{K}_{\theta i}^{-1}\boldsymbol{J}_{\theta i}^{T}) & \boldsymbol{J}_{pi} \\ \boldsymbol{J}_{pi}^{T} & \boldsymbol{0} \end{bmatrix} \begin{bmatrix} \bar{F}_{i,ext} \\ \Delta\bar{q}_{pi} \end{bmatrix} = \begin{bmatrix} \Delta\bar{X}_i \\ \bar{0} \end{bmatrix} \tag{1}$$

where $\boldsymbol{J}_{\theta i}$, and $\boldsymbol{J}_{pi}$ are the Jacobian matrices that are obtained by taking the partial derivative of the forward kinematic with respect to virtual, and passive joint variables. Accordingly, θ and p subscripts reflect the relation for virtual, and passive joint variables. $[\boldsymbol{K}_{\theta i}]_{6n\times 6n}$ denotes the non-diagonal structural stiffness matrix belonging to the i^{th} limb that has n links each defined in their respective link's frame. $[\bar{F}_{i,ext}]_{6\times 1}$ is the external force/torque vector carried by the i^{th} limb. $\bar{q}_{pi}$ contains passive joint variables. $\boldsymbol{0}$ in the left-hand side matrix contributes the zero-stiffness effect of passive joints.

The matrix at the left-hand side of Eq. 1 is a compliance matrix of the virtual and passive joints, namely $\boldsymbol{C}_i$. Taking the inverse of this matrix produces a stiffness matrix including the combined characteristics of the virtual and passive joints. A sub-matrix is extracted from the inverted $\boldsymbol{C}_i$ matrix which is a rank-deficient structural stiffness matrix, $\boldsymbol{K}_i$. This rank deficiency is a result of passive joints' zero-stiffness effect. The inversion is shown as follows:

$$\boldsymbol{C}_i = \begin{bmatrix} (\boldsymbol{J}_{\theta i}\boldsymbol{K}_{\theta i}^{-1}\boldsymbol{J}_{\theta i}^{T}) & \boldsymbol{J}_{pi} \\ \boldsymbol{J}_{pi}^{T} & \boldsymbol{0} \end{bmatrix} \quad \Rightarrow \boldsymbol{C}_i^{-1} = \left[\begin{array}{c:c} [\boldsymbol{K}_i]_{6\times 6} & \sim \\ \hdashline [\boldsymbol{K}_{pi}] & \sim \end{array}\right] \tag{2}$$

where upper-left 6×6 sub-part of the above inversion contains the desired Cartesian stiffness matrix, $\boldsymbol{K}_i$. $\boldsymbol{K}_{pi}$ gives the relation between the compliant deflections and passive joint motion. The compliance matrix is a function of joint variables. If the manipulator is not in a singular configuration or does not go into a singular pose after a compliant deflection, $\boldsymbol{C}_i$ is always invertible. The latter can occur in an iterative solution process.

In parallel mechanisms, limbs are represented as a 6-DoF spring. Parallel connected springs are directly summed up to compute the equivalent spring model as shown in Eq. 3. It is assumed that external force $\bar{F}_{ext}$ is known but the distribution of this force on the limbs is yet to be determined. Since all the limbs are connected at one node, the deflections are all equal. After solving Eq. 4 for $\Delta\bar{X}$, loads carried by each limb are computed as shown in Eq. 5.

$$\boldsymbol{K} = \sum_{i=1}^{n} \boldsymbol{K}_i, \quad \bar{F}_{ext} = \sum_{i=1}^{n} \bar{F}_{i,ext}, \quad \Delta\bar{X} = \Delta\bar{X}_1 = \Delta\bar{X}_2 = ... = \Delta\bar{X}_n \tag{3}$$

$$\bar{F}_{ext} = \boldsymbol{K}\Delta\bar{X} \tag{4}$$

$$\bar{F}_{i,ext} = \boldsymbol{K}_i\Delta\bar{X} \tag{5}$$

where $\bar{F}_{ext}$ external wrench applied on the mobile platform. $\boldsymbol{K}$ is the structural stiffness matrix of the manipulator.

Note that the matrix $\boldsymbol{C}_i$ is expressed symbolically. Computers may not handle this inversion operation. To obtain a quick solution, a numeric recursive computation is required.

The initial computation step of virtual joint variable column matrix, $\bar{\theta}_i = \bar{0}$ in $\boldsymbol{J}_{\theta i}$.

This first assignment gives a solution in which the external force/torque is distributed on the flexible bodies with respect to the undeflected states of the links. As the manipulator experiences a compliant displacement, the force/torque distribution changes accordingly. A back-substitution of the virtual and passive joint variables is required to consider this effect.

Once the compliant deflection, $\Delta\bar{X}$, is computed, Eq. 5 can be used. Solution of Eq. 6 gives the new $\bar{\theta}_i^{(k+1)}$ where k is the iteration number for $k = 0, 1, ...$ Superscript (0) denotes the state when there is no load on the manipulator. Finally, Eq. 7 gives the relaxation of passive joints.

$$\boldsymbol{K}_{\theta i}(\bar{\theta}_i^{(k)}, \bar{q}_{ai}^{(0)}, \bar{q}_{pi}^{(k)})[\bar{\theta}_i^{(k+1)} - \bar{\theta}_i^{(0)}] = [\boldsymbol{J}_i^T(\bar{\theta}_i^{(k)}, \bar{q}_{ai}^{(0)}, \bar{q}_{pi}^{(k)})]\bar{F}_{i,ext}^{(k)} \tag{6}$$

$$\bar{q}_{pi}^{(k+1)} - \bar{q}_{pi}^{(0)} = \boldsymbol{K}_{(pi)}(\bar{\theta}_i^{(k)}, \bar{q}_{ai}^{(0)}, \bar{q}_{pi}^{(k)})\bar{X}_i^{(k)} \tag{7}$$

where $\bar{q}_{ai}$ is a column matrix that contains active joint variables. Generally, it has only one element for parallel manipulators with a single actuator at each limb.

In a static loading case on the mobile platform, an iterative solution is obtained within 3 to 5 iterations [4]. However, this accuracy improvement is limited for simply-constrained and over-constrained parallel manipulators. Hence, direct computation is preferred.

3. Case study: Modified 6R Over-Constrained Parallel Mechanism

The over-constrained structure makes the stiffness modeling process more challenging due to several kinematic loop closures. Hence, a systematic modeling approach needs to be developed. Before the modeling process, some simplifications and assumptions must be made.

3.1. The Mechanism's Insight

A drawing of the mechanism is given in Fig. 1. There are 4 different types of links as shown in the Fig. 2. While Link 1 and Link 4 are made of aluminium alloy, Link 2 and Link 3 are combinations of aluminium parts and carbon fiber tubes to have a lighter manipulator. The tubes and aluminium parts are attached via pins and industrial glues. Bearings and retaining rings are made of stainless steel and assembled to Links 2 and 3. Multiple bearings are used on both sides of the aluminium parts for these links to minimize joint clearances. Thus, the following simplifications and assumptions are made in the stiffness model computations:

- The base and the mobile platform are made of thick aluminium alloy. Therefore, they are assumed to be rigid.
- Link 4 is made of aluminium and exposed to tension/compression forces. Therefore, it is assumed to be rigid since the part is highly stiff against these force types. It should be noted that this is not a general case for all parallelogram loops. If there is an assembly arrangement such as the one presented in [13], then all the links of a parallelogram may be considered as flexible.
- Links 2 and 3 are flexible due to thin carbon fiber tubes and the glue used for fixing the tubes and the aluminium parts.

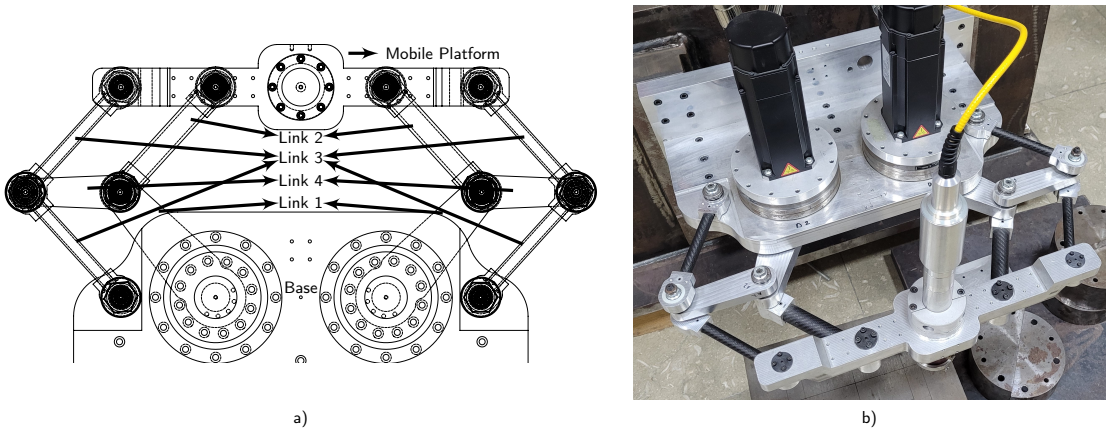

Figure 1: a) CAD sketch and link types of the manipulator, b) the manipulator.

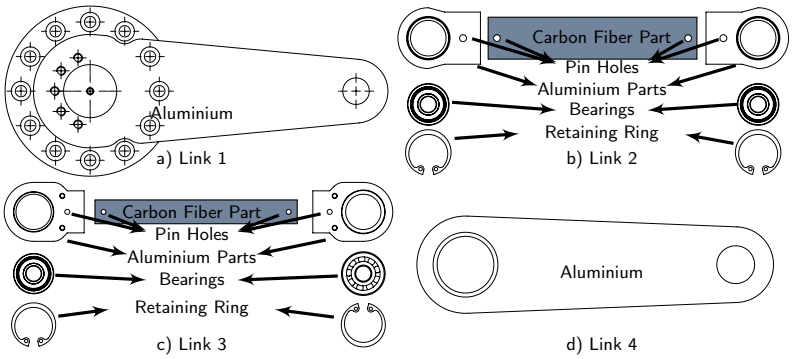

Figure 2: 4 types of links.

- The bearing/retaining rings are stiffened stainless steel. Therefore, these parts are assumed to be rigid.
- The manipulator is over-constrained. Therefore, the joint clearances are assumed to be negligible.
- Link 1 is the actuated link. However, this link is considerably thicker in the link group. Hence, it is relatively rigid. Nonetheless, the link is considered flexible to preserve the generality of the formulation. Its rigidity is achieved by assigning a high stiffness value which did not result in an observable effect in computations.
- Our main focus in this paper is the structural stiffness modeling of this mechanism. In a wider aspect, the stiffness of the actuation, bearings, balancing springs, and series elastic actuators can be considered. Those can be the subject of another research as a future study.

Next, we classify the forces/torques that are considered to compute compliant deflections. Since the manipulator has no force/torque interaction with an external object, effective force/torques are caused by dynamic effects and gravity. These are related to inertia. Hence, the followings are considered for mass and mass moment of inertia distribution:

- Accelerations at the mobile platform are up to 5g. Since dynamic effects are dominant, gravitational effects are excluded.
- Carbon fiber tubes of Links 2 and 3 are lightweight compared to their aluminium parts and bearings. Therefore, it can be assumed that the masses are accumulated at the proximal and distal ends of the links instead of the geometric center of the link. As a result, dynamic and gravitational forces/moments are generated at the connection nodes/joints of these links.
- Accumulated masses have a limited rotation, but linear accelerations of these masses are dominant. So, the inertial effects due to rotational motion can be neglected.

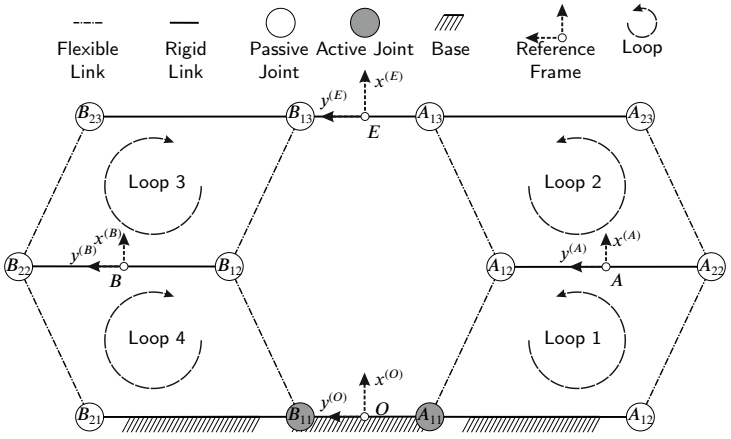

Figure 3: Kinematic sketch of modified 6R manipulator and its components.

- The mobile platform is assumed to have no rotation since the joint clearances are relatively small.
- Link 4 is assumed to have no rotation, and its mass is equally distributed on the connection nodes/joints.
- Compared to force/moment on the distal end of Link 1 that is caused by the motion of the mobile platform, dynamic forces/moments of Link 1, due to its inertial properties, are negligible.
- The kinematic motion of the manipulator is planar. Consequently, only two components of the resulting dynamic forces acting on the plane and the moment about the normal of this plane can be considered.

3.2. Stiffness Modeling Objectives

After all these analyses, it is possible to construct a simplified sketch of the manipulator for stiffness model computations as shown in Fig. 3. The main objective is to compute the compliant deflection of the mobile platform frame, $\mathcal{F}(E)$.

Note that the masses of the links are accumulated on the joints. The masses at the joints B_{21}, and A_{21} are not considered since they are at the base. Masses on B_{22}-B_{12}, and A_{12}-A_{22} pairs are rigidly connected to each other. In addition to the mobile platform mass, distributed mass groups of the links at B_{23}, B_{13}, A_{13}, and B_{23} joints are rigidly connected. The mass centers and also the geometric centers of these connections are located at the origins of frames $\mathcal{F}(E)$, $\mathcal{F}(B)$, and $\mathcal{F}(A)$ as shown in Fig. 3. These frames are the frames where the external forces/torques are generated due to the dynamic motion and the gravity. Even if there is only one force/torque on one of these frames, not only this frame's location, but also the other frame locations are affected since all links are connected. To compute this effect, there should be 3 stiffness models for all 3 frames. To compute these 3 stiffness models, a solution approach may adopt the divide-and-conquer strategy to overcome the modeling difficulties.

Considering the smallest sub-structures in Fig. 3, there are 4 sub-loops that are composed of parallelograms. Loops 1 and 4 are active loops that are connected to actuators. Loops 2 and 3 are the passive loops. Loop pair 1-4, and loop pair 2-3 have the same stiffness properties. If the stiffness model of each loop is obtained by connecting them first serially and then parallel to each other, it is possible to get stiffness matrices of the frames $\mathcal{F}(E)$, $\mathcal{F}(B)$, and $\mathcal{F}(A)$.

Let us name the stiffness matrices of the loops 1, 2, 3, and 4 as $\boldsymbol{K}_{L1}$, $\boldsymbol{K}_{L2}$, $\boldsymbol{K}_{L3}$, and $\boldsymbol{K}_{L4}$, respectively. Also, the resulting stiffness matrices for the frames $\mathcal{F}(E)$, $\mathcal{F}(B)$, and $\mathcal{F}(A)$ are called $\boldsymbol{K}_E$, $\boldsymbol{K}_B$, and $\boldsymbol{K}_A$, respectively. By considering the serial/parallel connections of the loops, desired stiffness models are represented in Fig. 4.

In summary, the sub-tasks that should be completed to obtain stiffness models can be listed as follows:

- Divide the mechanism into smaller parallelogram sub-loops.
- Obtain the stiffness model of each sub-loop. (Parallelogram loop level stiffness model)
- Obtain the stiffness model of each serial limb made up of serial connection of these sub-loops.
- Obtain the stiffness model of the entire mechanism by composing the stiffness models of each serial limb. (6R loop level stiffness model)

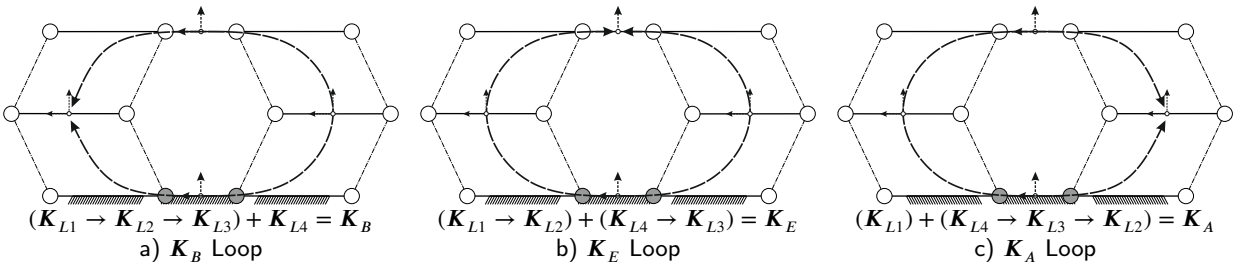

Figure 4: Stiffness loops of the frames where "→" and "+" show the serial and parallel connections, respectively.

3.3. Stiffness Model of the Parallelogram Loops

The first sub-task is to obtain stiffness matrices of both passive and active parallelograms. Fig. 5 shows a generic sketch of a parallelogram. Fig. 5 a) shows the actual VJM representation while b) shows the equivalent VJM stiffness model we seek. One important thing that should be noticed is the connection sequence of the joints and virtual joints (or virtual springs). As shown in Fig. 5 a), the virtual joints/springs are always located at the distal end of the link, but before the regular joint even-though both are coincident. However, these virtual joints do not contain any kinematic information, which means their stiffness information is given with respect to the local frames of the links. A stiffness model combined with the kinematic model is obtained when the stiffness model of the parallelogram is formulated relative to the fixed frame. Then, it can be represented as a single 6-DoF spring as shown in Fig. 5 b). Note that this is a virtual kinematic chain representing the stiffness properties as the actual one.

The compliant kinematics of parallelogram is formulated by Eqs. 8 and 9. Eq. 10 shows the compliant kinematic model equivalent of the parallelogram. In Eq. 11, kinematic constraints are given.

$$\boldsymbol{H}_1 = \boldsymbol{T}_y(d/2)\boldsymbol{R}_z(\varphi_{11})\boldsymbol{T}_x(l_1)\boldsymbol{H}_v(\bar{\theta}_{11'})\boldsymbol{R}_z(\varphi_{12})\boldsymbol{T}_y(-d/2) \tag{8}$$

$$\boldsymbol{H}_2 = \boldsymbol{T}_y(-d/2)\boldsymbol{R}_z(\varphi_{21})\boldsymbol{T}_x(l_1)\boldsymbol{H}_v(\bar{\theta}_{21'})\boldsymbol{R}_z(\varphi_{22})\boldsymbol{T}_y(d/2) \tag{9}$$

$$\boldsymbol{H}_{Eq} = \boldsymbol{R}_z(\varphi_1)\boldsymbol{T}_x(l_1)\boldsymbol{R}_z(-\varphi_1)\boldsymbol{H}_v(\bar{\theta}_{2'}) \tag{10}$$

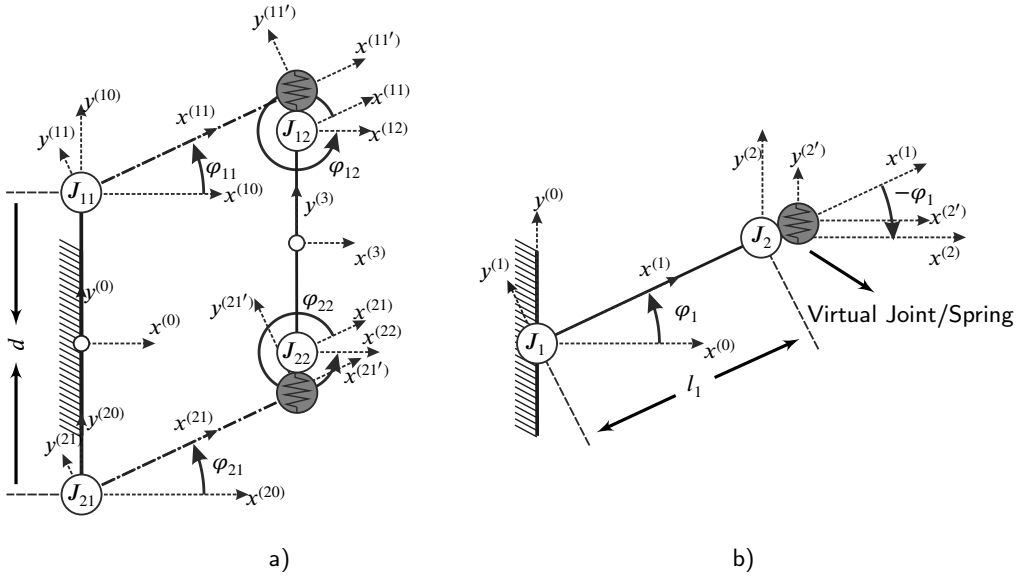

Figure 5: Stiffness model sketches. a) Actual the VJM sketch of the parallelogram b) Resultant the VJM equivalent of the parallelogram. Superscripts and subscripts (ij), and (j) denote the j^{th} joint frame in i^{th} limb for $i, j = 1, 2$, and $'$ represents the virtual joint frame.

$$\varphi_{11} = \varphi_{21}, \quad \varphi_{12} = \varphi_{22}, \quad \varphi_{11} + \varphi_{12} = \varphi_{21} + \varphi_{22} = 2\pi k \quad \text{for} \quad k = 1, 2, ... \tag{11}$$

where $\boldsymbol{H}_1$, $\boldsymbol{H}_2$, and $\boldsymbol{H}_{Eq}$ are the compliant kinematic models of upper, and lower limbs and parallelogram's equivalent. $\boldsymbol{R}_{x,y,z}$ and $\boldsymbol{T}_{x,y,z}$ denote the pure rotation and translation homogeneous transformation matrices about/along x, y, z axes. d is the distance between the joints J_{11} and J_{21}, while l_1 is the link length. φ_{11}, φ_{12}, φ_{21}, and φ_{22} are the joint variables. Depending on the computed parallelogram loop, φ_{11} and/or φ_{21} might be active or passive joints. $\bar{\theta}_{11'}$, $\bar{\theta}_{21'}$, and $\bar{\theta}_{2'}$ denote the column matrices of 6 virtual joint variables in their respective limbs. Due to the rigid connections at the connection frame $\mathcal{F}(3)$ in Fig. 5 a), $\boldsymbol{H}_1 = \boldsymbol{H}_2 = \boldsymbol{H}_{Eq}$ and also, compliant displacements of these frames for both limbs are the same, $\Delta\boldsymbol{H}_1 = \Delta\boldsymbol{H}_2 = \Delta\boldsymbol{H}_{Eq}$.

The stiffness model computations differ depending on whether there are active and/or passive joints, or not. In the following sections, the formulations are given.

3.3.1. Stiffness of an Active Parallelogram Loop

In this section, the stiffness model of the active parallelogram loop, $\boldsymbol{K}_{Eq(active)}$, is given. This matrix corresponds to our $\boldsymbol{K}_{L1}$ and $\boldsymbol{K}_{L4}$ loops' stiffness matrices. The joint J_{11} is taken as the active joint. Given this statement, the joint variables are re-organized in column matrix form as follows:

$$\bar{Q}_1 = \begin{bmatrix} \bar{\theta}_{11'}^T & q_{a1} & q_{p1} \end{bmatrix}_{8\times1}^T, \quad q_{a1} = \begin{bmatrix} \varphi_{11} \end{bmatrix}_{1\times1}, \quad q_{p1} = \begin{bmatrix} \varphi_{12} \end{bmatrix}_{1\times1} \tag{12}$$

$$\bar{Q}_2 = \begin{bmatrix} \bar{\theta}_{21'}^T & \bar{q}_{p2} \end{bmatrix}_{8\times1}^T, \quad \bar{q}_{p2} = \begin{bmatrix} \varphi_{21} & \varphi_{22} \end{bmatrix}_{2\times1}^T \tag{13}$$

$$\bar{Q}_{Eq} = \begin{bmatrix} \bar{\theta}_{2'}^T & \varphi_1 \end{bmatrix}_{7\times1}^T \tag{14}$$

Next, Jacobian matrices $\boldsymbol{J}_{\theta1}, \boldsymbol{J}_{\theta2}, \boldsymbol{J}_{\theta Eq}, \bar{J}_{a1}, \bar{J}_{p1}, \boldsymbol{J}_{p2}, \bar{J}_{aEq}, \boldsymbol{J}_1, \boldsymbol{J}_2$, and $\bar{J}_{Eq}$ are computed considering the forward kinematics equation given in Eqs. 8 to 10, and joint variables presented Eqs. 12 to 14.

Active, passive, and virtual joint-related Jacobian matrices of the upper chain and equivalent model of the parallelogram are presented in Eq. 15, assuming that $\bar{\theta}_{11'} = \bar{0}$. Considering $\bar{\theta}_{2'} = \bar{0}$, $\bar{J}_{\theta Eq}$ is computed as 6×6 identity matrix meaning that it emulates the DoF of its equivalent spring. This is logical since the equivalent model merely represents the actual one.

$$\boldsymbol{J}_{\theta1} = \begin{bmatrix} c_{a1} & -s_{a1} & 0 & 0 & 0 & \frac{d}{2} \\ s_{a1} & c_{a1} & 0 & 0 & 0 & 0 \\ 0 & 0 & 1 & \frac{-dc_{a1}}{2} & \frac{ds_{a1}}{2} & 0 \\ 0 & 0 & 0 & c_{a1} & -s_{a1} & 0 \\ 0 & 0 & 0 & s_{a1} & c_{a1} & 0 \\ 0 & 0 & 0 & 0 & 0 & 1 \end{bmatrix}, \quad \begin{bmatrix} \bar{J}_{a1} & \bar{J}_{p1} \end{bmatrix} = \begin{bmatrix} \frac{d}{2} - l_1 s_{a1} & \frac{-d}{2} \\ l_1 c_{a1} & 0 \\ 0 & 0 \\ 0 & 0 \\ 0 & 0 \\ 1 & -1 \end{bmatrix}, \quad \bar{J}_{aEq} = \begin{bmatrix} -l_1 \sin(\varphi_1) \\ l_1 \cos(\varphi_1) \\ 0 \\ 0 \\ 0 \\ 0 \end{bmatrix} \tag{15}$$

In Eq. 15, c_{a1} and s_{a1} denote the cosine(φ_{11}) and sine(φ_{11}) functions, respectively. $\boldsymbol{J}_{\theta2}$ and $\boldsymbol{J}_{p2}$ are similar to $\boldsymbol{J}_{\theta1}$ and $\begin{bmatrix} \bar{J}_{a1} & \bar{J}_{p1} \end{bmatrix}$ matrices but d and φ_{11} are replaced with $-d$ and φ_{21}, respectively. $\bar{J}_{aEq}$ indicates that the distal end of the single link equivalence has no rotational property but linear displacements in xy-plane, only. This means that the equivalent model only positions the virtual spring at the distal end.

Inversion operation in Eq. 2 for both upper and lower limbs is carried out to obtain the stiffness matrices $\boldsymbol{K}_1$ and $\boldsymbol{K}_2$. When the lower limb is individually considered with its kinematic constraints, it has 1 DoF that is uncontrollable due to the passive joints. This generates a zero-resistance direction. Hence, it can freely move when a force is applied that is tangent to its path. Therefore, the rank of $\boldsymbol{K}_2$ is 5. However, $\boldsymbol{K}_1$ is full rank. Finally, $\boldsymbol{K}_1$ and $\boldsymbol{K}_2$ stiffness matrices are summed to obtain $\boldsymbol{K}_{Eq(active)}$ according to Eq. 3 and given as follows:

$$\boldsymbol{K}_{Eq(active)} = \boldsymbol{K}_1 + \boldsymbol{K}_2 \tag{16}$$

Equivalent stiffness matrices of upper and lower limbs, $\boldsymbol{K}_1$ and $\boldsymbol{K}_2$, can be procured experimentally or by performing finite element analysis. A parametric definition of these matrices is possible, but the inversion operation in Eq. 2 may not be succeeded. Yet, it is still possible to obtain an inversion for $\bar{\theta}_{11'} = \bar{0}$, $\bar{\theta}_{21'} = \bar{0}$ and a specific set of values for the angles φ_{11} and φ_{21}. For $\varphi_{11} = 0$, the stiffness of the upper limb, $\boldsymbol{K}_1$, is represented in Eq. 17 where the k terms are the elements of $\boldsymbol{K}_1$. The stiffness matrix $\boldsymbol{K}_2$ is similar to $\boldsymbol{K}_1$ but the variable d is replaced with $-d$, and the element in 2nd row-2nd column is zero, and elements k are updated according to the stiffness of the lower limb.

$$\boldsymbol{K}_1 = \begin{bmatrix} k_{11}^{(1)} & 0 & 0 & 0 & 0 & -\frac{d}{2}k_{11}^{(1)} \\ 0 & k_{22}^{(1)} - \frac{(k_{26}^{(1)})^2}{k_{66}^{(1)}} & 0 & 0 & 0 & 0 \\ 0 & 0 & k_{33}^{(1)} & \frac{d}{2}k_{33}^{(1)} & k_{35}^{(1)} & 0 \\ 0 & 0 & \frac{d}{2}k_{33}^{(1)} & \frac{d^2}{4}k_{33}^{(1)} + k_{44}^{(1)} & \frac{d}{2}k_{35}^{(1)} & 0 \\ 0 & 0 & k_{35}^{(1)} & \frac{d}{2}k_{35}^{(1)} & k_{55}^{(1)} & 0 \\ -\frac{d}{2}k_{11}^{(1)} & 0 & 0 & 0 & 0 & \frac{d^2}{4}k_{11}^{(1)} \end{bmatrix} \tag{17}$$

3.3.2. Stiffness of a Passive Parallelogram Loop

In this section, the stiffness model of the passive parallelogram loop, $\boldsymbol{K}_{Eq(passive)}$, is given. This matrix corresponds to our $\boldsymbol{K}_{L2}$ and $\boldsymbol{K}_{L3}$ loops' stiffness matrices. Compared to the active parallelogram, the computation of the stiffness of a passive parallelogram changes only by taking $\boldsymbol{J}_{11}$ as a passive joint. The corresponding joint variables are updated as follows:

$$\bar{Q}_1 = \begin{bmatrix} \bar{\theta}_{11}^T, & \bar{q}_{p1}^T \end{bmatrix}_{8\times1}^T, \quad \bar{q}_{p1} = \begin{bmatrix} \varphi_{11} & \varphi_{12} \end{bmatrix}_{2\times1}^T \tag{18}$$

Calculations of Eqs. 2 and 3 are straightforward for generating stiffness matrix for passive parallelogram $\boldsymbol{K}_{Eq(passive)}$. This matrix is a rank-deficient matrix with a rank of 5.

While computing the stiffness of the parallelograms, stiffness matrices of the links are treated as joint space stiffness matrices since the links are the sub-structures of the parallelograms. Similarly, parallelograms are the sub-loops of the whole manipulator. Hence, their stiffness matrices are treated as joint space stiffness matrices of the manipulator. If the stiffness matrices of parallelograms have full rank, the computation in Eq. 2 would be applicable. However, this computation for passive sub-loops is not possible since they are rank deficient. To overcome this problem, a fictitious stiffness element can be included for the component of $\boldsymbol{K}_{Eq(passive)}$ to deal with the rank deficiency. Another approach is to reduce the virtual joint DoF from 6 to 5 for the passive manipulators' equivalent model. Both methods require manual modification in stiffness and Jacobian matrix elements. This process can be tedious if there are several passive loops as sub-loops. To preserve the straightforward methodology, $\boldsymbol{J}_{11}$ and $\boldsymbol{J}_{21}$ are both considered as active joints to obtain a full rank stiffness matrix of $\boldsymbol{K}_{Eq(passive)}$. The passive joint effect is later viewed in the stiffness model computation of the whole manipulator when connecting the loops [4]. Consequently, the following joint variable set is constructed:

$$\bar{Q}_1 = \begin{bmatrix} \bar{\theta}_{11}^T, & q_{a1} & q_{p1} \end{bmatrix}_{8\times1}^T, \quad q_{a1} = \begin{bmatrix} \varphi_{11} \end{bmatrix}_{1\times1}, \quad q_{p1} = \begin{bmatrix} \varphi_{12} \end{bmatrix}_{1\times1} \tag{19}$$

$$\bar{Q}_2 = \begin{bmatrix} \bar{\theta}_{21}^T, & q_{a2} & q_{p2} \end{bmatrix}_{8\times1}^T, \quad q_{a2} = \begin{bmatrix} \varphi_{21} \end{bmatrix}_{1\times1}, \quad q_{p2} = \begin{bmatrix} \varphi_{22} \end{bmatrix}_{1\times1} \tag{20}$$

Next, the new stiffness matrix, $\boldsymbol{K}_{Eq(passive)}$, is computed assuming both upper and lower limbs have active first joints $\boldsymbol{J}_{11}$ and $\boldsymbol{J}_{21}$. The new stiffness matrix, $\boldsymbol{K}_2$, is similar to $\boldsymbol{K}_1$ in Eq. 17 except the variable d is replaced with $-d$. If both the upper and lower links have the same link designs, $\boldsymbol{K}_{Eq(passive)} = \boldsymbol{K}_1 + \boldsymbol{K}_2$ summation results in $2\boldsymbol{K}_1$ but the parameters with d vanishes due to $\pm$ signs and the elements without d and with d^2 are doubled. In our case study, this is not necessary since upper and lower limbs have different designs.

3.4. Stiffness Model of the Manipulator

In this section, it is shown how $\boldsymbol{K}_{Eq(active)}$ and $\boldsymbol{K}_{Eq(passive)}$ matrices are correlated with each other to obtain the stiffness model of the manipulator. The stiffness matrices belonging to the frames $\mathcal{F}(E)$, $\mathcal{F}(B)$, and $\mathcal{F}(A)$ are presented. These matrices are $\boldsymbol{K}_E$, $\boldsymbol{K}_B$, and $\boldsymbol{K}_A$ matrices, respectively. Using the equivalent stiffness model of the parallelograms, the compliant kinematics of these frames are illustrated in Fig. 6. The steps are listed below, and a flow chart is shown in Fig. 7..

1. In Eqs. 21-27, the compliant forward kinematics are constructed. $\boldsymbol{H}$ is the kinematic model. Sub-indices A, B, E indicate the belonging frames of the kinematic models. Sub-indices $1, 2$ denote the right and left limbs up to these frames, respectively.

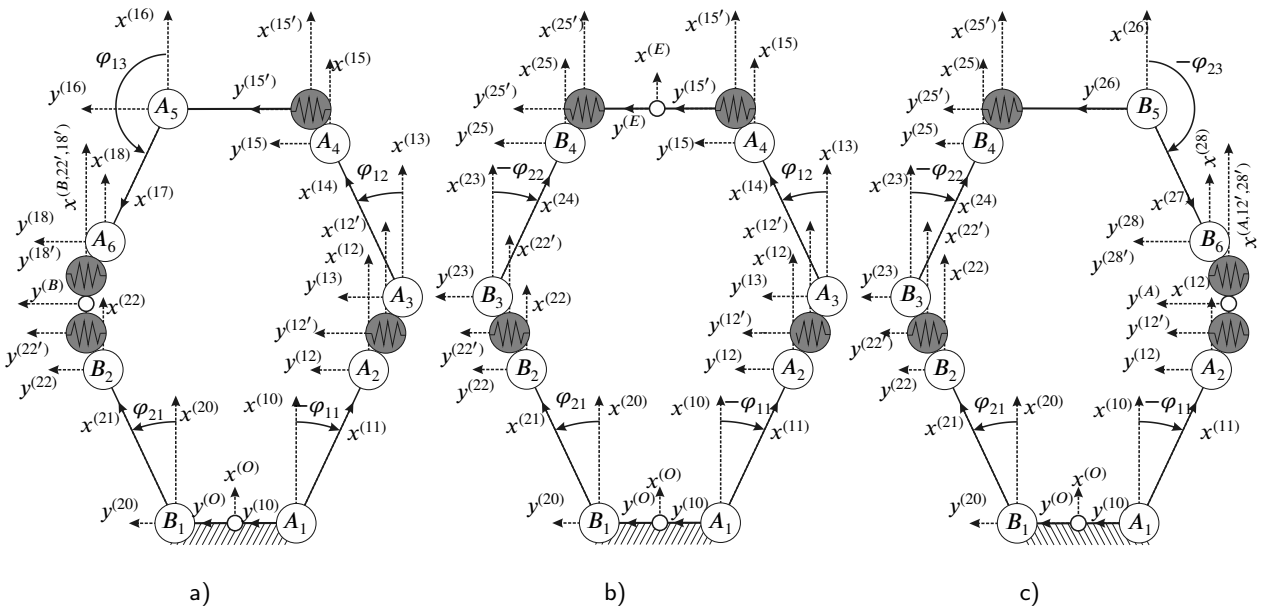

Figure 6: Stiffness model illustrations of the frames: a) $\mathcal{F}(B)$ b) $\mathcal{F}(E)$ c) $\mathcal{F}(A)$.

2. In Eqs. 28-33, the joint variable column matrices are defined, and passive/active joint variables are grouped.
3. The forward kinematic models and grouped joint variables are used to obtain the required Jacobian matrices. These Jacobian matrices are $\boldsymbol{J}_{\theta B1}$, $\boldsymbol{J}_{\theta B2}$, $\boldsymbol{J}_{\theta A1}$, $\boldsymbol{J}_{\theta A2}$, $\boldsymbol{J}_{\theta E1}$, $\boldsymbol{J}_{\theta E2}$, $\bar{\boldsymbol{J}}_{aB1}$, $\bar{\boldsymbol{J}}_{aB2}$, $\bar{\boldsymbol{J}}_{aA1}$, $\bar{\boldsymbol{J}}_{aA2}$, $\bar{\boldsymbol{J}}_{aE1}$, $\bar{\boldsymbol{J}}_{aE2}$, $\boldsymbol{J}_{pB1}$, $\bar{\boldsymbol{J}}_{pE1}$, $\bar{\boldsymbol{J}}_{pE2}$, and $\boldsymbol{J}_{pA2}$ are obtained. Again, sub-indices θ, a, p denote that the Jacobian matrix is derived with respect to the virtual, active, and passive joint variables. Here, $\bar{q}_p$ column matrices help us to obtain $\bar{\boldsymbol{J}}_p$ Jacobian matrices. These Jacobian matrices consider the passive joints' zero stiffness effect in the further computation steps. Therefore, we can correct the mathematical manipulation of $\boldsymbol{K}_{Eq(passive)}$ being full rank.
4. In Eqs. 34-39, stiffness matrices of $\boldsymbol{K}_{Eq(active)}$ and $\boldsymbol{K}_{Eq(passive)}$ are used to obtain the joint space stiffness matrices of the limbs. Since each parallelogram is reduced to a single link representation, each limb's joint space stiffness matrix contains a number of these $\boldsymbol{K}_{Eq(active)}$ and $\boldsymbol{K}_{Eq(passive)}$ matrices. $\boldsymbol{K}_{\theta}$ denotes that the matrix is the joint space stiffness matrix, and the remaining sub-indices show the belonging frame and followed limb route.
5. Now, the inversion operation in Eq. 2 can be held by relating the Jacobian matrices in step 3 and Joint space stiffness matrices in Eqs. 34-39. This inversion produces $\boldsymbol{K}_{A1}$, $\boldsymbol{K}_{A2}$, $\boldsymbol{K}_{B1}$, $\boldsymbol{K}_{B2}$, $\boldsymbol{K}_{E1}$, and $\boldsymbol{K}_{E2}$ stiffness matrices of each limb in Cartesian space. Finally, by connecting each limb at its respective frame, in Eq. 40, the Cartesian space stiffness matrix of each frame $\boldsymbol{K}_{A}$, $\boldsymbol{K}_{B}$, and $\boldsymbol{K}_{E}$ are obtained.

Note that the serial connection of parallelogram loops is mathematically represented by Eq. 2. This equation provides the mathematical basis for connecting the $\mathcal{F}(3)$ frame of the proximal loop to $\mathcal{F}(0)$ frame of the distal loop in Fig. 5 a). In other words, the coupler link of the proximal loop becomes coincident with the base link of the distal loop at $\mathcal{F}(0) - \mathcal{F}(3)$ frames.

$$\boldsymbol{H}_{B1} = \boldsymbol{T}_y(-d/2)\boldsymbol{R}_z(-\varphi_{11})\boldsymbol{T}_x(l_1)\boldsymbol{R}_z(\varphi_{11})\boldsymbol{H}_v(\bar{\theta}_{12'})\boldsymbol{R}_z(\varphi_{12})\boldsymbol{T}_x(l_1)\boldsymbol{R}_z(-\varphi_{12})\boldsymbol{H}_v(\bar{\theta}_{15'})... \\ ...\boldsymbol{T}_y(d)\boldsymbol{R}_z(\varphi_{13})\boldsymbol{T}_x(l_1)\boldsymbol{R}_z(-\varphi_{13})\boldsymbol{H}_v(\bar{\theta}_{18'}) \tag{21}$$

$$\boldsymbol{H}_{B2} = \boldsymbol{T}_y(d/2)\boldsymbol{R}_z(\varphi_{21})\boldsymbol{T}_x(l_1)\boldsymbol{R}_z(-\varphi_{21})\boldsymbol{H}_v(\bar{\theta}_{22'}) \tag{22}$$

$$\boldsymbol{H}_{E1} = \boldsymbol{T}_y(-d/2)\boldsymbol{R}_z(-\varphi_{11})\boldsymbol{T}_x(l_1)\boldsymbol{R}_z(\varphi_{11})\boldsymbol{H}_v(\bar{\theta}_{12'})\boldsymbol{R}_z(\varphi_{12})\boldsymbol{T}_x(l_1)\boldsymbol{R}_z(-\varphi_{12})\boldsymbol{H}_v(\bar{\theta}_{15'})\boldsymbol{T}_y(d/2) \tag{23}$$

$$\boldsymbol{H}_{E2} = \boldsymbol{T}_y(d/2)\boldsymbol{R}_z(\varphi_{21})\boldsymbol{T}_x(l_1)\boldsymbol{R}_z(-\varphi_{21})\boldsymbol{H}_v(\bar{\theta}_{22'})\boldsymbol{R}_z(-\varphi_{22})\boldsymbol{T}_x(l_1)\boldsymbol{R}_z(\varphi_{22})\boldsymbol{H}_v(\bar{\theta}_{25'})\boldsymbol{T}_y(-d/2) \tag{24}$$

$$\boldsymbol{H}_{A1} = \boldsymbol{T}_y(-d/2)\boldsymbol{R}_z(-\varphi_{11})\boldsymbol{T}_x(l_1)\boldsymbol{R}_z(\varphi_{11})\boldsymbol{H}_v(\bar{\theta}_{12'}) \tag{25}$$

$$\boldsymbol{H}_{A2} = \boldsymbol{T}_y(d/2)\boldsymbol{R}_z(\varphi_{21})\boldsymbol{T}_x(l_1)\boldsymbol{R}_z(-\varphi_{21})\boldsymbol{H}_v(\bar{\theta}_{22'})\boldsymbol{R}_z(-\varphi_{22})\boldsymbol{T}_x(l_1)\boldsymbol{R}_z(\varphi_{22})\boldsymbol{H}_v(\bar{\theta}_{25'})... \\ ...\boldsymbol{T}_y(-d)\boldsymbol{R}_z(-\varphi_{23})\boldsymbol{T}_x(l_1)\boldsymbol{R}_z(\varphi_{23})\boldsymbol{H}_v(\bar{\theta}_{28'}) \tag{26}$$

$$\boldsymbol{H}_{B1} = \boldsymbol{H}_{B2}, \quad \boldsymbol{H}_{E1} = \boldsymbol{H}_{E2}, \quad \boldsymbol{H}_{A1} = \boldsymbol{H}_{A2}, \quad \varphi_{21} = \varphi_{12}, \quad \varphi_{11} = \varphi_{22}, \quad \varphi_{13} + \varphi_{11} = \varphi_{23} + \varphi_{21} = \pi \tag{27}$$

$$\bar{Q}_{B1} = \begin{bmatrix} \bar{\theta}_{B1}^T & q_{aB1} & \bar{q}_{pB1}^T \end{bmatrix}_{21\times1}^T, \; q_{aB1} = \varphi_{11}, \; \bar{q}_{pB1}^T = \begin{bmatrix} \varphi_{12} & \varphi_{13} \end{bmatrix}^T, \; \bar{\theta}_{B1} = \begin{bmatrix} \bar{\theta}_{12'}^T & \bar{\theta}_{15'}^T & \bar{\theta}_{18'}^T \end{bmatrix}_{18\times1}^T \tag{28}$$

$$\bar{Q}_{B2} = \begin{bmatrix} \bar{\theta}_{B2}^T & q_{aB2} \end{bmatrix}_{7\times1}^T, \; q_{aB2} = \varphi_{21}, \; \bar{\theta}_{B2} = \bar{\theta}_{22'} \tag{29}$$

$$\bar{Q}_{E1} = \begin{bmatrix} \bar{\theta}_{E1}^T & q_{aE1} & q_{pE1} \end{bmatrix}_{14\times1}^T, \; q_{aE1} = \varphi_{11}, \; q_{pE1} = \varphi_{12}, \; \bar{\theta}_{E1} = \begin{bmatrix} \bar{\theta}_{12'}^T & \bar{\theta}_{15'}^T \end{bmatrix}_{12\times1}^T \tag{30}$$

$$\bar{Q}_{E2} = \begin{bmatrix} \bar{\theta}_{E2}^T & q_{aE2} & q_{pE2} \end{bmatrix}_{14\times1}^T, \; q_{aE2} = \varphi_{21}, \; q_{pE2} = \varphi_{22}, \; \bar{\theta}_{E2} = \begin{bmatrix} \bar{\theta}_{22'}^T & \bar{\theta}_{25'}^T \end{bmatrix}_{12\times1}^T \tag{31}$$

$$\bar{Q}_{A1} = \begin{bmatrix} \bar{\theta}_{A1}^T & q_{aA1} \end{bmatrix}_{7\times1}^T, \; q_{aA1} = \varphi_{11}, \; \bar{\theta}_{A1} = \bar{\theta}_{12'} \tag{32}$$

$$\bar{Q}_{A2} = \begin{bmatrix} \bar{\theta}_{A2}^T & q_{aA2} & \bar{q}_{pA2}^T \end{bmatrix}_{21\times1}^T, \; q_{aA2} = \varphi_{21}, \; \bar{q}_{pA2}^T = \begin{bmatrix} \varphi_{22} & \varphi_{23} \end{bmatrix}^T, \; \bar{\theta}_{A2} = \begin{bmatrix} \bar{\theta}_{22'}^T & \bar{\theta}_{25'}^T & \bar{\theta}_{28'}^T \end{bmatrix}_{18\times1}^T \tag{33}$$

$$\boldsymbol{K}_{\theta B1} = diag\left(\boldsymbol{K}_{Eq(active)}, \boldsymbol{K}_{Eq(passive)}, \boldsymbol{K}_{Eq(passive)}\right)_{18\times18} \tag{34}$$

$$\boldsymbol{K}_{\theta B2} = diag\left(\boldsymbol{K}_{Eq(active)}\right)_{6\times6} \tag{35}$$

$$\boldsymbol{K}_{\theta E1} = diag\left(\boldsymbol{K}_{Eq(active)}, \boldsymbol{K}_{Eq(passive)}\right)_{12\times12} \tag{36}$$

$$\boldsymbol{K}_{\theta E2} = diag\left(\boldsymbol{K}_{Eq(active)}, \boldsymbol{K}_{Eq(passive)}\right)_{12\times12} \tag{37}$$

$$\boldsymbol{K}_{\theta A1} = diag\left(\boldsymbol{K}_{Eq(active)}\right)_{6\times6} \tag{38}$$

$$\boldsymbol{K}_{\theta A2} = diag\left(\boldsymbol{K}_{Eq(active)}, \boldsymbol{K}_{Eq(passive)}, \boldsymbol{K}_{Eq(passive)}\right)_{18\times18} \tag{39}$$

$$\boldsymbol{K}_B = \boldsymbol{K}_{B1} + \boldsymbol{K}_{B2}, \quad \boldsymbol{K}_E = \boldsymbol{K}_{E1} + \boldsymbol{K}_{E2}, \quad \boldsymbol{K}_A = \boldsymbol{K}_{A1} + \boldsymbol{K}_{A2} \tag{40}$$

3.5. The Displacement of the Mobile Platform due to Compliant Deflections of Flexible Links

The deflection of the coordinate frame of the mobile platform $\mathcal{F}(E)$, that is caused by the forces acting on this frame, $\bar{F}_E$, is defined as $\Delta\bar{X}_E^{(E)}$. The lower index indicates the frame where the deflections occur, and the upper index shows the location of the force causing this deflection. In this regard, loads acting on $\mathcal{F}(A)$ and $\mathcal{F}(B)$ frames cause $\Delta\bar{X}_E^{(A)}$ and $\Delta\bar{X}_E^{(B)}$ deflections in the $\mathcal{F}(E)$ frame.

To compute the deflection contribution of the forces acting on $\mathcal{F}(A)$ and $\mathcal{F}(B)$ to the frame $\mathcal{F}(E)$, first, the deflections in joint space (virtual and passive) are computed. The virtual and passive joint variables are $[\bar{\theta}_{B1}, \bar{q}_{pB1}]$ for $\mathcal{F}(B)$ and $[\bar{\theta}_{A2}\bar{q}_{pA2}]$ for $\mathcal{F}(A)$ frames.

The resulting total deflection in $\mathcal{F}(E)$ is computed by superposing all these deflections as follows:

$$\Delta\bar{X}_E = \Delta\bar{X}_E^{(E)} + \Delta\bar{X}_E^{(B)} + \Delta\bar{X}_E^{(A)} \tag{41}$$

The computation of each element is listed as follows:

1. $\Delta\bar{X}_E^{(E)}$ is computed as shown in Eq. 42.
2. Eq. 43 shows the deflection of the frame $\mathcal{F}(A)$ that is caused by the forces acting on this frame. The frame $\mathcal{F}(E)$ is included in the 2nd limb of $\mathcal{F}(A)$. Therefore, compliant kinematics of this limb is used.
3. Eq. 44 shows the deflections in 2nd limb's passive joints, $\Delta\bar{q}_{pA2}$, of $\mathcal{F}(A)$. Here, $\boldsymbol{K}_{pA2}$ is computed via Eq. 2.
4. In Eq. 45, $\boldsymbol{K}_{A2}\Delta\bar{X}_A$ represents the distributed force of $\bar{F}_A$ on 2nd limb. By multiplying this force with $\boldsymbol{J}_{\theta A2}^T$, it is transformed into joint space indicated as $\boldsymbol{J}_{\theta A2}^T\boldsymbol{K}_{A2}\Delta\bar{X}_A$. Then, change in virtual joints, $\Delta\bar{\theta}_{A2}$, are computed by multiplying the joint space force with $\boldsymbol{K}_{\theta A2}^{-1}$.
5. After obtaining both passive and virtual joint values of 2nd limb, they are used in compliant forward kinematics to acquire the deflection in $\mathcal{F}(E)$ caused by the forces acting on $\mathcal{F}(A)$.
6. However, $\bar{\theta}_{A2}$ has 18 virtual joint variables and $\bar{q}_{pA2}$ has 2 passive joint variables. To conduct the computation, variables in $\bar{\theta}_{A2}$ and $\bar{q}_{pA2}$ should be chosen that corresponds to 2nd limb. The first 12 variables of $\bar{\theta}_{A2}$ are selected and shown as $\bar{\theta}_{A2,1-12}$. Similarly, the first element of $\bar{q}_{pA2}$ is shown by $\bar{q}_{pA2}(1)$.

7. Finally, the deflection, $\Delta\bar{X}_E^{(A)}$, is calculated in Eq. 46. $\boldsymbol{J}_{E2}$ is the Jacobian matrix of 2nd limb that is defined up to $\mathcal{F}(E)$ which includes 12 virtual joints and 1 passive joint.
8. Computations for $\Delta\bar{X}_E^{(B)}$ are given in Eqs. 47-50.

$$\Delta\bar{X}_E^{(E)} = \boldsymbol{K}_E^{-1}\bar{F}_E \tag{42}$$
$$\Delta\bar{X}_A^{(A)} = \boldsymbol{K}_A^{-1}\bar{F}_A \tag{43}$$
$$\Delta\bar{q}_{pA2} = \boldsymbol{K}_{pA2}\Delta\bar{X}_A \tag{44}$$
$$\Delta\bar{\theta}_{A2} = \boldsymbol{K}_{\theta A2}^{-1}\boldsymbol{J}_{\theta A2}^T\boldsymbol{K}_{A2}\Delta\bar{X}_A \tag{45}$$
$$\Delta\bar{X}_E^{(A)} = \boldsymbol{J}_{E2}\Delta\bar{\theta}_{A2,1-12} + \boldsymbol{J}_{pE2}\Delta\bar{q}_{pA2,1} \tag{46}$$
$$\Delta\bar{X}_B^{(B)} = \boldsymbol{K}_B^{-1}\bar{F}_B \tag{47}$$
$$\Delta\bar{q}_{pB1} = \boldsymbol{K}_{pB1}\Delta\bar{X}_B \tag{48}$$
$$\Delta\bar{\theta}_{B1} = \boldsymbol{K}_{\theta B1}^{-1}\boldsymbol{J}_{\theta B1}^T\boldsymbol{K}_{B1}\Delta\bar{X}_B \tag{49}$$
$$\Delta\bar{X}_E^{(B)} = \boldsymbol{J}_{E1}\Delta\bar{\theta}_{B1,1-12} + \boldsymbol{J}_{pE1}\Delta\bar{q}_{pB1,1} \tag{50}$$

3.6. Summary of Stiffness Modelling

A brief summary of the computation steps is given as follows:

1. Determine the active and the passive sub-loops. Active loops are attached to the base frame, and passive loops are located between the active loops and the mobile platform.
2. Calculate the stiffness matrices of active and passive loops as described in Sections 3.3.1 and 3.3.2. Now, the parallelograms are reduced to a single-link representation.
3. Determine the frames at which loads are applied. There are two auxiliary frames $\mathcal{F}(A)$ and $\mathcal{F}(B)$, and one mobile platform frame $\mathcal{F}(E)$ as shown in Fig. 6.
4. Perform a serial connection representation of an active and a number of passive loops until these frames. It is a serial connection of an active and a passive loop for the mobile platform frame for both limbs. For auxiliary frames, an active loop is followed by two passive loops at one limb, while the other limb only consists of a single active loop. Serial connection is denoted by "→" in Figs. 4 and 7.
5. For each limb, construct the forward kinematics of reduced parallelograms up to these frames as given in Eqs. 21 to 27 including the active, passive, and virtual joints of reduced parallelograms. We need to develop two forward kinematics formulations for each loading frame since each frame has 2 limbs. In total, 6 forward kinematic models are acquired. Next, construct the Jacobian matrices of these forward kinematic models of each limb.
6. Construct the diagonal stiffness matrix model of serially connected reduced parallelograms as given in Eqs. 34 to 39.
7. Connect each limb parallel to the other. This is a simple summation of stiffness models obtained in the previous step and shown in Eq. 40. Now, $\boldsymbol{K}_E$, $\boldsymbol{K}_A$, and $\boldsymbol{K}_B$ are obtained. This parallel connection is denoted by "+" in Figs. 4 and 7. The first column in Fig. 7 summarizes all the computations including this step..
8. Compute the compliant deflection of each loading frame as shown in the second column of Fig. 7.
9. Perform the computations in Section 3.5 to obtain the compliant deflection of the mobile platform caused by the loads applied at the loading frames. This is the final column of Fig. 7.

4. Simulation, Results, and Discussion

The procured stiffness model is coded in MATLAB Simulink, and simulation tests are conducted. Then, the obtained results are compared with the finite element analysis (FEA) results considering the results obtained via ANSYS Workbench. This section presents the results of this verification via comparison.

The stiffness parameters of the links (shown in Fig. 2) are determined via experiments by applying loads and measuring the compliant deflections with a coordinate measuring machine (CMM) FARO Prime Arm 1.2. Forcing combinations along 3-axes are applied to generate deflections at the distal ends of each link. Complaint deflections at

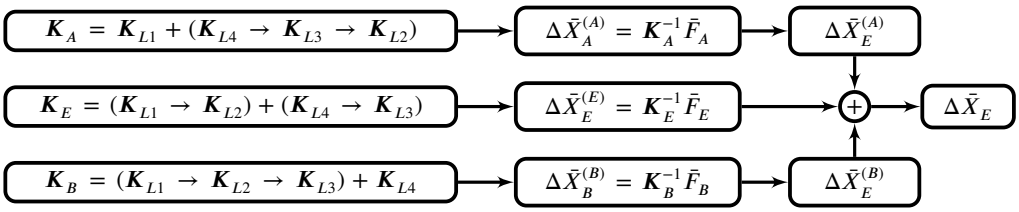

Figure 7: Computation chart to obtain the deflections in frame $\mathcal{F}(E)$.

distal ends are captured via CMM (see Fig. 10 a) and b)). Deflections in Link 1 are smaller than the tolerance range of the CMM ($\pm$0.023 mm); hence, a high stiffness value is assigned to this link's stiffness matrix, $\boldsymbol{K}_{\theta 1}$. Also, it is considered as a rigid body in the FEM. Based on the experimental data, the local stiffness matrices of Link 2,$\boldsymbol{K}_{\theta 2}$, and Link 3, $\boldsymbol{K}_{\theta 3}$, are computed as given below by relating the deflections to the forcing. The computation is achieved by minimizing $\Delta\bar{F} - \boldsymbol{K}\Delta\bar{X}$ for each test data. Since the format of $\boldsymbol{K}$ is known, optimization for 8 elements of $\boldsymbol{K}$ was sufficient. The units of the stiffness matrix components for upper left-right and lower left-right 3×3 sub-matrices are N/m, N/rad, N·m/m, and N·m/rad, respectively.

$$\boldsymbol{K}_{\theta 2} = \begin{bmatrix} 92317585 & 0 & 0 & 0 & 0 & 0 \\ 0 & 418506 & 0 & 0 & 0 & -31388 \\ 0 & 0 & 418506 & 0 & 31388 & 0 \\ 0 & 0 & 0 & 604 & 0 & 0 \\ 0 & 0 & 31388 & 0 & 3139 & 0 \\ 0 & -31388 & 0 & 0 & 0 & 3139 \end{bmatrix} \tag{51}$$

$$\boldsymbol{K}_{\theta 3} = \begin{bmatrix} 17040334 & 0 & 0 & 0 & 0 & 0 \\ 0 & 77250 & 0 & 0 & 0 & -5794 \\ 0 & 0 & 77250 & 0 & 5794 & 0 \\ 0 & 0 & 0 & 111 & 0 & 0 \\ 0 & 0 & 5794 & 0 & 579 & 0 \\ 0 & -5794 & 0 & 0 & 0 & 579 \end{bmatrix} \tag{52}$$

$$\boldsymbol{K}_{\theta 1} = 10^6 \cdot \boldsymbol{K}_{\theta 2} \tag{53}$$

The manipulator's stiffness model is analyzed at 9 test points. Since the manipulator has a symmetric behaviour about the x-axis, the test points are chosen at one side of the workspace, namely, along the positive y-axis (see Fig. 3). The workspace dimensions are 100 mm $\times$ 150 mm along x-y axes. The home position of the workspace is located at (212.3 mm, 0 mm) with respect to $\mathcal{F}(O)$ which corresponds to the $\varphi_{21} = 45°, \varphi_{11} = -45°$ values of the active joint angles. The test points and the joint angles are given in Fig. 8.

The manipulator is designed to work at 5g acceleration range. With the laser emitter mounted on the mobile platform, the combined mass is 5 kg. The mass of the Link 4 group is 1 kg. By taking the gravitational acceleration $g = 10 m/s^2$ as numerical simplification, the maximum external forces on the bodies are 250 N for the mobile platform and 25 N for the intermediate link group. The values of force assignments are insignificant for comparing the FEA and the VJM results. The aim is to analyze the stiffness model at an instant in which the maximum dynamic forces occur by making use of D'Alembert's principle. Analyses are conducted for dynamic forces acting on 2 intermediate ($\mathcal{F}_{(A)}$, $\mathcal{F}_{(B)}$) and 1 mobile platform ($\mathcal{F}_{(E)}$) terminals on xy-plane, simultaneously. These 3 force vectors are parallel to each other. The forces are applied in 6 different directions. These vectors start along the x-axis and divide a half rotation into 6 parts. Hence, between each consecutive force vector, there is 30° difference.

The FEA was conducted in the "Static Structural" tool of ANSYS Workbench. To match the experimentally identified stiffness matrices $\boldsymbol{K}_{\theta 2}$, and $\boldsymbol{K}_{\theta 3}$ a new material was defined via assigning Young's modulus value in ANSYS Workbench. Another option could have been to change the link designs to comply with the stiffness values. The base, mobile platform, Link 4, and Link 1 are defined as rigid bodies under the "Geometry" section of "Static Structural", while the remaining bodies were elastic. At each link's distal and proximal ends, "Remote Point" was defined. These nodes were fixed to meshes at the distal and proximal ends. This helps us to track the compliant deflections of distal and proximal ends of each link in 6-DoF. The connection of the links was utilized over the remote points by defining

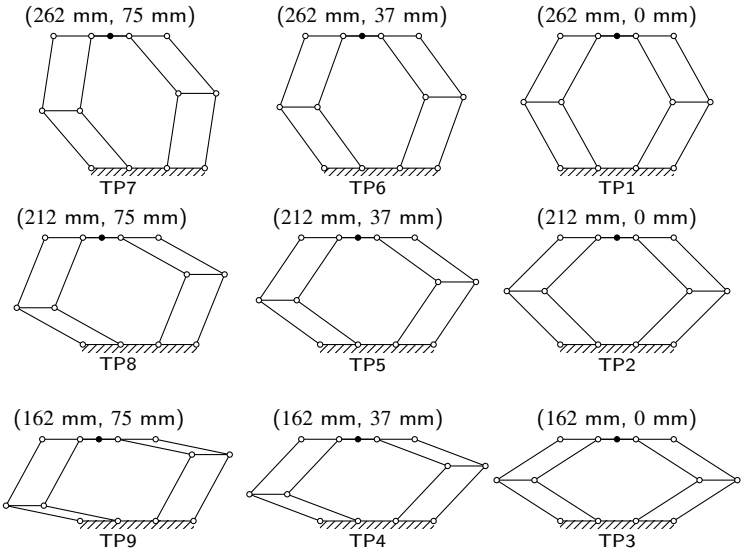

TP	$\varphi_{11}(^\circ)$	$\varphi_{21}(^\circ)$	x (mm)	y (mm)
1	-29	29	262	0
2	-45	45	212	0
3	-57.3	57.3	162	0
4	-43.3	69.3	162	37
5	-34.1	54.1	212	37
6	-19.9	36.1	262	37
7	-8.7	40.6	262	75
8	-22	60.9	212	75
9	-28.6	78.3	162	75

Figure 8: Illustration of test points (TP) and their corresponding active joint angles.

Table 1
The FEA setup details of ANSYS Workbench.

Mesh Properties	
Size Function	Curvature
Relevance Center	Fine
Transition	Slow
Span Angle Center	Fine
Curvature Normal Angle	18°
Min Size	2mm
Max Face Size	4mm
Max Tet Size	5mm
Growth Rate	Default
Remaining Parameters	Default
Element Type	Quad4
	SHELL181

Analysis Settings	
Solver Target	Mechanical APDL
Solver Type	Iterative
Weak Springs	On
Spring Stiffness	Program Controlled
Solver Pivot Check	Program Controlled
Large Deflection	On
Newton-Raphson	Program Controlled
Force Convergence	On
Moment Convergence	On
Displacement Convergence	On
Rotation Convergence	On
Tolerance	0.05%
Minimum Reference	0.001N, 0.001Nm, 0m, 0°

the "Revolute" joint option. To use the FEA in its highest accuracy, the "Iterative" solver option was selected, and "Large Deflections" were activated. Further details are given in Table 1.

The compliant deflections calculated via the FEA for forces acting on $\mathcal{F}_{(A)}$, $\mathcal{F}_{(B)}$, and $\mathcal{F}_{(E)}$ are grouped under FEA_{EAB} label, and compliant deflections calculated via the VJM are labeled as VJM_{EAB}. In addition, VJM_{E} is considered a force acting on $\mathcal{F}_{(E)}$ only. By comparing these three compliant deflection results, we can comment on the performance of the proposed superposition methodology, VJM_{EAB}, over the traditional one, VJM_{E}. The results are given in Appendix A. To evaluate the performance more practically, the results are further summarized by averaging the magnitudes of the compliant deflections for all force directions. The summarized results are given in Table 2. A percent error term is defined below to determine if the superposition methodology, VJM_{EAB}, is superior with respect to VJM_{E}, or not.

$$e_E = (|FEA_{\text{EAB}} - VJM_{\text{E}}|/FEA_{\text{EAB}}) \times 100 \tag{54}$$

$$e_{EAB} = (|FEA_{\text{EAB}} - VJM_{\text{EAB}}|/FEA_{\text{EAB}}) \times 100 \tag{55}$$

It can be observed in Table 2 that overall accuracy for the calculation of y-axis deflections via VJM_{EAB} compared to VJM_{E} is better while x-axis deflection estimation accuracy of VJM_{EAB} is relatively worse. Specifically, x-axis performance of VJM_{EAB} is lower at test points 1, 2, 3, and 9. The first three points are located along the symmetry axis, and the 9^{th} point is positioned at a corner of the workspace. A point on the symmetry axis corresponds to a special configuration, and a corner point is closer to the singular configuration of the manipulator. Hence, extreme performance

Table 2
Summarized deflection results for the FEA and the VJM.

Test Point	$\mathbf{FEA_{EAB}}$ $\Delta x(\mu m)$	$\mathbf{VJM_{E}}$ $\Delta x(\mu m)$	$\mathbf{VJM_{EAB}}$ $\Delta x(\mu m)$	e_{xE} %	e_{xEAB} %	$\mathbf{FEA_{EAB}}$ $\Delta y(\mu m)$	$\mathbf{VJM_{E}}$ $\Delta y(\mu m)$	$\mathbf{VJM_{EAB}}$ $\Delta y(\mu m)$	e_{yE} %	e_{yEAB} %
1	1.1	1	1.2	4.7	14.1	41.6	41.7	41.7	0.2	0.2
2	1.6	1.5	1.8	5.2	10.3	20.8	20.9	20.9	0.3	0.3
3	2.8	2.7	3.1	3.6	12.1	14.7	14.7	14.7	0.1	0.1
4	15.8	16.2	16	2.5	1.2	19.1	19.7	19.1	3.2	0.1
5	7.5	7.5	7.5	0.2	0.7	23.1	23.2	23.1	0.7	0.1
6	8.7	8.7	8.7	0.0	0.4	48.6	48.8	48.7	0.3	0.2
7	20.7	20.8	20.8	0.2	0.2	61.1	61.3	61.3	0.4	0.2
8	17.6	17.9	17.7	1.6	0.8	26.6	27.1	26.6	2.1	0.2
9	71	72.4	68.6	2.0	3.4	35.5	36.6	34.8	2.9	2.2

increments/decrements or no contribution might be expected at these points. Compared to $\mathrm{VJM_E}$, $\mathrm{VJM_{EAB}}$ did not improve further the error term at test points 5, 6, 7 for x-axis and 1, 2, 3 for y-axis. Finally, x-axis performance at test points 4, 8, and y-axis performance at test points 4 to 9 are increased when the proposed methodology is used. In short, when the new method ($\mathrm{VJM_{EAB}}$) was used, performance increased in eight conditions, remained the same in six conditions, and got worse in four conditions among the nine x and nine y-axis deflections conditions. It is possible to use the superposition methodology for y-axis deflections and the regular methodology ($\mathrm{VJM_E}$) for x-axis deflection computation. Note that the stiffness model computation of serially connected parallelograms presented in this paper are still used in both cases. The computation cost for running the stiffness model for one node (i.e. $\mathcal{F}_{(E)}$) is examined. It is measured that it can run at 10kHz on a computer with Dual Intel Xeon E5-2600 processor and 16GB ECC RDIMM Memory at running at 1600MHz.

Note that the manipulator operates in a 2-DoF motion space (2 translations). However, the actual manipulator has loop assemblies at different heights (see Fig. 1 b) and 9 b)). The height difference between the distal and proximal parallelograms are not considered in this part. Nonetheless, the presented calculation procedure and acquired stiffness model via the VJM are developed using 6-DoF virtual joints. Since the VJM model and the FEA simulation model are developed with this procedure, their results validate each other.

5. Experimental Procedure for Model Parameter Update

In the experimental study, the mobile platform is subjected to external static loads to generate compliant deflections. Only the static forces acting at the end-effector are considered; hence, no dynamic loads acts on the manipulator resulting in auxiliary forces at A and B nodes. Consequently, $\mathrm{VJM_E}$ model is found to be suitable for tuning its parameters via this experimental study since it excludes the other A and B nodes and superposition methodology. In the actuator system, Kollmorgen AKM33E brushless servo motors with built-in brake and Sumitomo Fine Cyclo F1C-A15 gearbox are used. Built-in brakes of the servo motor are used to lock the mechanism. At the loading conditions, the brakes of the actuator are on and actuation stiffness is not considered. Next, measurements are taken via FARO Prime Arm 1.2 model CMM. Then, the stiffness parameters are optimized to minimize the error between the model and experiment data. The mobile platform location has two conditions: pre-load and post-load. Pre-load condition is formulated as shown below

$$\bar{X}_M^{(1)} = \bar{X}_R^{(1)} + \bar{X}_G^{(1)} + \bar{X}_I^{(1)} + \bar{X}_J^{(1)} \tag{56}$$

where $\bar{X}_M^{(1)}$ is the position vector of the mobile platform frame with respect to the base frame. This vector is computed via CMM measurements, and it can be decomposed into a set of vector summations. $\bar{X}_R^{(1)}$ is the position vector computed by rigid body forward kinematics. $\bar{X}_G^{(1)}$ is the deflection caused by gravity. $\bar{X}_I^{(1)}$ is the compliant deflection contribution of internal stresses due to the over-constrained structure. $\bar{X}_J^{(1)}$ is the joint clearance contributions. The upper index 1 indicates the initial state, i.e., pre-load state.

When the load is applied on the mobile platform, the mechanism switches from state 1 to state 2 which can be expressed as follows:

$$\bar{X}_M^{(2)} = \bar{X}_R^{(2)} + \bar{X}_G^{(2)} + \bar{X}_I^{(2)} + \bar{X}_J^{(2)} + \bar{X}_E^{(2)} \tag{57}$$

$$\Delta\bar{X}_M = \bar{X}_M^{(2)} - \bar{X}_M^{(1)} \tag{58}$$

$\bar{X}_E$ is deflection caused by external force applied on the mobile platform. Superscript 2 indicates the post-load state. $\Delta\bar{X}_M$ suggests the change in position between the states. $\bar{X}_R$ is calculated by using the encoder data connected to the actuator. Since the actuators are locked, $\Delta\bar{X}_R = \bar{0}$. It is known that parallel mechanisms reduce the adverse effect of joint clearances; hence, $\Delta\bar{X}_J = \bar{0}$ is assumed. The most significant drawback of an over-constrained mechanism is its high internal stresses. These internal stresses are caused by the geometrical errors of the manufactured parts. Our mechanism was produced with high production precision. In addition, special hinge construction is used to tolerate a possible geometric error, and a particular assembling procedure is followed when fastening the connection screws. Although these precautions help reduce internal stresses, they cannot be fully neglected. Hence, $\Delta\bar{X}_I \neq \bar{0}$. Due to the compliant kinematic state change, the compliant deflection caused by gravity differs in the first and second position states. Since the applied load on the mobile platform is much greater than the change in gravitational loading from the first to second position state, $\Delta\bar{X}_G = \bar{0}$ can be assumed. As a result, the first and second position states are simplified,and a force/compliant deflection equation is written as follows:

$$\bar{F} = \boldsymbol{K}_C \Delta\bar{X}_M = \boldsymbol{K}_C(\Delta\bar{X}_I + \bar{X}_E) \tag{59}$$

Stiffness model $\boldsymbol{K}_C$ is a function of the local stiffness matrices $\boldsymbol{K}_{\theta 1}$, $\boldsymbol{K}_{\theta 2}$, and $\boldsymbol{K}_{\theta 3}$, and the joint variables φ_{11} and φ_{21}. $\varphi_{11}, \varphi_{21}$ variables are determined by the controller for the desired trajectory. The parameters of these local stiffness matrices need to be updated in accordance with the compliant deflection of the mobile platform. This update is achieved by adding a symmetric modification matrix to the local stiffness matrices, which has 21 parameters to be determined. The modification matrix can also be considered a measure of deviation from the original stiffness values of the link. This deviation can be caused by the contribution of the shaft, bearing, bolt, fastening torque of the screws, and internal stresses. As mentioned earlier, $\boldsymbol{K}_{\theta 1}$ is assumed to be highly stiff. Therefore, a total of 42 parameters must be determined for $\boldsymbol{K}_{\theta 2}$, and $\boldsymbol{K}_{\theta 3}$. The parameter update is defined as follows:

$$\boldsymbol{K}'_{\theta 2} = \boldsymbol{K}_{\theta 2} + \begin{bmatrix} k_1 & k_7 & k_{12} & k_{16} & k_{19} & k_{21} \\ k_7 & k_2 & k_8 & k_{13} & k_{17} & k_{20} \\ k_{12} & k_8 & k_3 & k_9 & k_{14} & k_{18} \\ k_{16} & k_{13} & k_9 & k_4 & k_{10} & k_{15} \\ k_{19} & k_{17} & k_{14} & k_{10} & k_5 & k_{11} \\ k_{21} & k_{20} & k_{18} & k_{15} & k_{11} & k_6 \end{bmatrix}, \quad \boldsymbol{K}'_{\theta 3} = \boldsymbol{K}_{\theta 3} + \begin{bmatrix} k_{22} & k_{28} & k_{33} & k_{37} & k_{40} & k_{42} \\ k_{28} & k_{23} & k_{29} & k_{34} & k_{38} & k_{41} \\ k_{33} & k_{29} & k_{24} & k_{30} & k_{35} & k_{39} \\ k_{37} & k_{34} & k_{30} & k_{25} & k_{31} & k_{36} \\ k_{40} & k_{38} & k_{35} & k_{31} & k_{26} & k_{32} \\ k_{42} & k_{41} & k_{39} & k_{36} & k_{32} & k_{27} \end{bmatrix} \tag{60}$$

where superscript $'$ denotes the updated stiffness matrices. The units of the modification matrix components for upper left-right and lower left-right 3×3 sub-matrices are N/m, N/rad, N·m/m, and N·m/rad, respectively. The links of the manipulator are located at different positions along the z-axis, as shown in Fig. 9 b). These position differences are not considered in the modeling. Since the position along z-axis is constant for all parts, connection shafts along the z-axis make a constant contribution to local stiffness matrices and they are not a function of joint variables. The effect of this continious contribution of z-axis offset can be carried out by the modification matrices necessary to comply with the experiment data. Hence, the existing model can be used.

Another contribution of the modification matrices is acquiring the internal stress-related stiffness model. Internal stress behaves like a compressed/stretched spring that depends on the kinematic states of the manipulator. In addition, applied external force contributes to the internal stresses by further compression/tension. Therefore, $\boldsymbol{K}_C$ in Eq. 59 can be updated to contain internal stiffness parameters, $\boldsymbol{K}_I$, as follows:

$$\boldsymbol{K}'_C = \boldsymbol{K}_C + \boldsymbol{K}_I \tag{61}$$

Acquisition of $\boldsymbol{K}_I$ requires an additional stiffness model for internal stresses as a function of kinematics which is a tedious process. Instead, we separate the stiffness model $\boldsymbol{K}_I$ into two parts. The first part, $\boldsymbol{K}_{Iv}$, is the variable part that changes with the mechanism's configuration. $\boldsymbol{K}_{Ic}$ is the constant part, and $\boldsymbol{K}_I = \boldsymbol{K}_{Iv} + \boldsymbol{K}_{Ic}$. $\boldsymbol{K}_{Iv}$ part is already infused in $\boldsymbol{K}'_{\theta 2}$ and $\boldsymbol{K}'_{\theta 3}$ while determining the modification matrix. For the constant $\boldsymbol{K}_{Ic}$ part, a new symmetric set of stiffness coefficients with 21 elements are defined. These coefficients are specified in the optimization process along with modification matrices.

$$\boldsymbol{K}'_C = \boldsymbol{K}_C(\boldsymbol{K}_{\theta 1}, \boldsymbol{K}'_{\theta 2}, \boldsymbol{K}'_{\theta 3}) + \boldsymbol{K}_{Ic}, \quad \boldsymbol{K}_{Ic} = \begin{bmatrix} k_{43} & k_{49} & k_{54} & k_{58} & k_{61} & k_{63} \\ k_{49} & k_{44} & k_{50} & k_{55} & k_{59} & k_{62} \\ k_{54} & k_{50} & k_{45} & k_{51} & k_{56} & k_{60} \\ k_{58} & k_{55} & k_{51} & k_{46} & k_{52} & k_{57} \\ k_{61} & k_{59} & k_{56} & k_{52} & k_{47} & k_{53} \\ k_{63} & k_{62} & k_{60} & k_{57} & k_{53} & k_{48} \end{bmatrix} \tag{62}$$

A final modification is issued for the external force applied on the mobile platform. Since there is a positional difference along the z-axis between the links, as shown in Fig. 9 b), external force, $\bar{F}$, generates a moment on the links. Our planar stiffness model cannot capture this effect. Nonetheless, the external force can be adapted for the stiffness model by introducing virtual vertical moment arms that will generate the same torsional effect on the links. Hence, the external force is updated as follows:

$$\bar{F} = \begin{bmatrix} F_x & F_y & 0 & 0 & 0 & 0 \end{bmatrix}^T \quad \rightarrow \bar{F}' = \begin{bmatrix} F_x & F_y & 0 & h_1 F_y & h_2 F_x & 0 \end{bmatrix}^T \tag{63}$$

where $\bar{F}$ is the actual external force applied on the mobile platform, and $\bar{F}'$ is the modified force. h_1 and h_2 are the moment arms in m determined in the model fitting process along with modification matrices. Including the stiffness matrix coefficients and moment arms, there are 65 parameters to be determined by the model-fitting algorithm.

The objective function to fit the model to the experimental data is defined as follows:

$$\bar{e} = \boldsymbol{K}'^{-1}_C \bar{F}' - \Delta \bar{X}_{\text{Measured}}, \quad E = \left\| \bar{e}_{1-5} \right\|, \quad E_{net} = \sum_{1}^{45} E \tag{64}$$

where $\bar{e}$ is the error vector between the modeled and measured deflection. E is the norm of the error vector's first 5 elements. The final element for z-axis rotation is excluded since it is not possible to measure the rotation of this axis with the measurement points in Fig. 9 b) which are aligned along the z-axis. Note that this introduces redundancy to the optimization, which searches for a suitable parameter set for the 5-DoF system using the 6-DoF stiffness model. Hence, the obtained result may not be unique. E_{net} is the objective function to be minimized, which is the summation of error norms through 45 measurements. The solution of the objective function is achieved via MATLAB by using *fmincon* and *fminsearch* functions. Initial values for parameters are defined between 0-1 randomly.

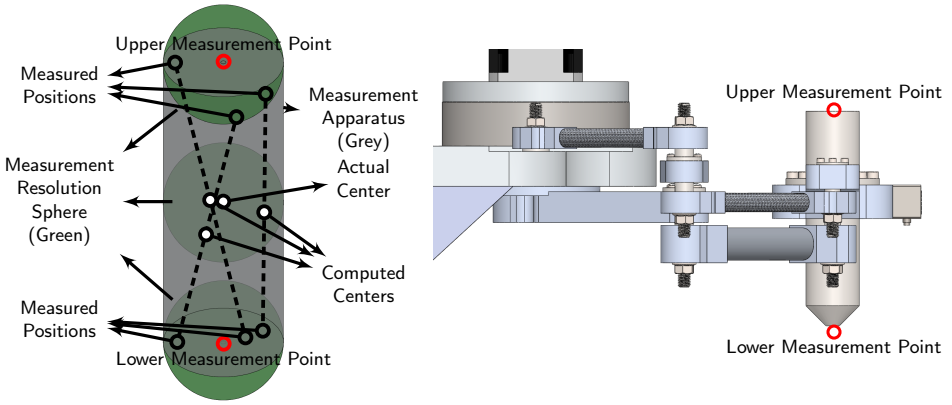

Figure 9: a) Illustration of measurements from the apparatus, b) $-y$-axis view of the manipulator.

5.1. Processing the Experiment Data

Experiment measurements need to be collected from the mobile platform frame origin, but it is impossible to reach this point with the CMM tip (ceramic spherical measuring tip). Therefore, a measurement apparatus was designed

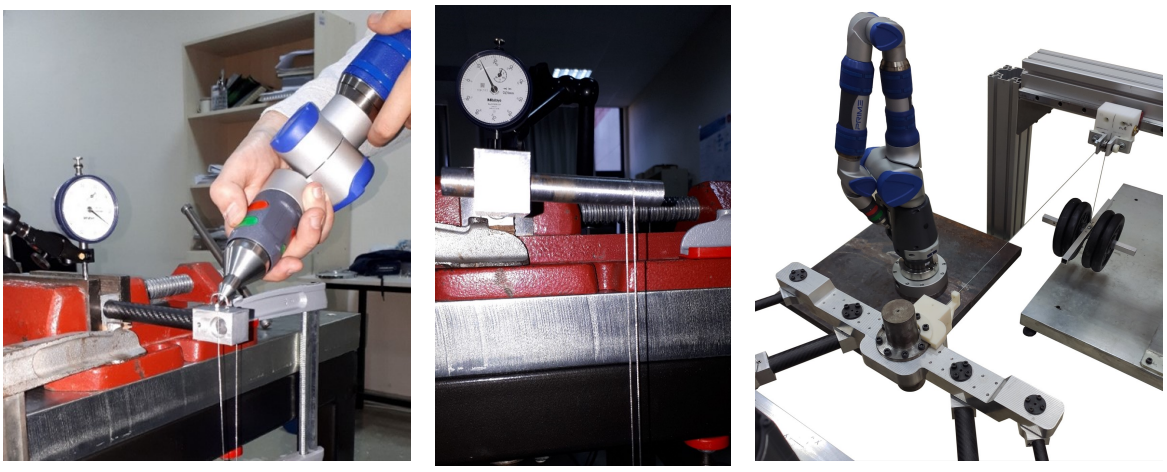

a) b) c)

Figure 10: a) Measurement of linear deflection via CMM for force load, b) applied torsion with a moment arm, c) load applied on the manipulator [30].

as a dummy tool for the mobile platform. There are upper and lower measurement points on the apparatus. With the location data collected from these points, the position of the mobile platform frame can be calculated. The resolution of the FARO Prime Arm 1.2 CMM, on which the test measurements were made, is ±0.023 mm. This means that the actual location of a point measured in space can be anywhere within a sphere with a radius of 0.023 mm. So when calculating the position of the mobile platform frame, this calculation has a margin of error of ±0.023 mm. The actual center of the mobile platform and the calculated centers are visualized in Fig. 9 a).

15 test points are determined in the workspace. Blocks with 5, 10, 15, 20, and 25 kg masses are used for loading and applied separately along x- and y-axes. These masses generate 49.05, 98.1, 147.15, 196.2, and 245.25 N loads, respectively. The coordinates of the mobile platform frame are measured via CMM once at each test point and for each loading case. Including the no-load case measurement, 6 measurements are recorded at each test point. By subtracting the measured coordinates of the dummy tool during the loaded case from measurements during the no-load case, 5 compliant deflection values are obtained for 5 to 25 kg loading cases. Thus, 75 deflection data are obtained for each x- and y-axes loading case. The experiment setup is shown in Fig. 10 and details are described in [30].

The stiffness model of this manipulator has the same absolute eigenvalues about the x-axis at the symmetric positions. For example, the absolute eigenvalue is the same at the (220 mm, -50 mm) and (220 mm, 50 mm) positions, meaning the same amount of compliant deflection should be observed for the same loading from the mobile platform frame. Nevertheless, the experimental data do not show a symmetrical feature. This is because the measurement accuracy of the CMM is not high enough. If a post-processing procedure is carried out to make the data obtained around the x-axis symmetrical, it is seen that the most significant error between the symmetric data set and the actual data set is smaller than ±0.023 mm. The amount of correction required for this process is defined as:

$$W = \left(\left| |V_{\text{Measured,Left}}| - |V_{\text{Measured,Right}}| \right| \right) /2 \tag{65}$$

$$V_{\text{Measured,Left}} \pm W = V_{\text{Measured,Right}} \mp W \tag{66}$$

Here W is the symmetry correction value, and V is the measured data. Measurements made on the right and left sides of the x-axis are compared with each other's kinematic symmetry, and new symmetrical values are obtained. When this correction is applied, the most considerable modification required to make the data obtained in the x-axis deflection experiments symmetrical is 0.0098 mm and 0.0217 mm for the y-axis. The largest change in angular deflections is 0.005° for x-axis rotation and 0.0085° for y-axis rotation. Therefore, it can be concluded that the cause of the symmetry error is due to the low resolution of the CMM. The symmetrical data set significantly facilitates fitting the model to the data. There are two reasons for this. The first is that the symmetrical state is closer to the ideal state, thus more mathematically suitable for calculations. The second is that about half of the data required to update the

Table 3
Average RMS error of model output and experimental data with updated and non-updated stiffness model parameters at loading conditions.

	Updated Model - F_x Load				Updated Model - F_y Load			
Load (N)	Δx (μm)	Δy (μm)	Δz (μm)	$\Delta\theta_y$ (°)	Δx (μm)	Δy (μm)	Δz (μm)	$\Delta\theta_x$ (°)
49.05	4.2	4.6	8.6	2×10^{-3}	5.1	5.7	5.0	3×10^{-3}
98.1	4.0	3.7	5.7	2×10^{-3}	5.5	2.2	10.3	2×10^{-3}
147.15	5.7	8.1	8.6	2×10^{-3}	7.6	5.2	11.2	2×10^{-3}
196.2	7.1	10.0	6.8	1×10^{-3}	8.1	5.5	11.5	2×10^{-3}
245.25	8.3	10.7	5.6	2×10^{-3}	10.7	5.9	13.6	2×10^{-3}

	Non-Updated Model - F_x Load				Non-Updated Model - F_y Load			
Load (N)	Δx (μm)	Δy (μm)	Δz (μm)	$\Delta\theta_y$ (°)	Δx (μm)	Δy (μm)	Δz (μm)	$\Delta\theta_x$ (°)
49.05	42.3	39.0	18.8	20×10^{-3}	39.6	172.7	4.9	10×10^{-3}
98.1	86.4	77.5	33.6	30×10^{-3}	78.9	351.4	10.6	20×10^{-3}
147.15	130.8	118.3	50.6	50×10^{-3}	121.6	526.4	11.7	20×10^{-3}
196.2	175.3	151.6	66.9	70×10^{-3}	159.5	699.8	11.9	30×10^{-3}
245.25	217.7	188.9	83.8	80×10^{-3}	201.0	879.5	13.8	40×10^{-3}

Table 4
Average absolute error between the model and experimental data for all loading conditions. The same upper index symbol indicates the symmetric test points.

			F_x Load				F_y Load			
Test Point	φ_{11}(°)	φ_{21}(°)	$e_x(\mu m)$	$e_y(\mu m)$	$e_z(\mu m)$	$e_{\theta y}$(°)	$e_x(\mu m)$	$e_y(\mu m)$	$e_z(\mu m)$	$e_{\theta x}$(°)
$1^{\dagger}$	-27.7	74.8	1.37	5.43	4.45	2×10^{-3}	2.45	5.38	15.24	1×10^{-3}
$2^{\star}$	-19.9	57.3	6.71	4.15	1.18	1×10^{-3}	7.30	2.48	12.26	2×10^{-3}
$3^{\bullet}$	-4.4	35.2	3.59	4.59	2.94	1×10^{-3}	6.56	2.78	8.12	3×10^{-3}
$4^{\otimes}$	-15.9	31.6	1.64	2.44	3.11	1×10^{-3}	7.41	3.85	8.37	3×10^{-3}
$5^{\triangle}$	-31.7	50.9	4.22	13.69	12.89	3×10^{-3}	3.52	1.67	5.75	2×10^{-3}
6°	-41.7	66.3	2.44	7.11	1.76	1×10^{-3}	3.52	2.67	6.40	1×10^{-3}
7	-55.0	55.0	7.81	0.86	5.43	1×10^{-3}	13.12	8.56	6.46	1×10^{-3}
8	-42.2	42.2	12.09	0.69	6.48	1×10^{-3}	2.81	6.34	9.09	2×10^{-3}
9	-24.9	24.9	5.04	0.46	4.31	2×10^{-3}	8.10	5.54	10.21	3×10^{-3}
10°	-66.3	41.7	2.59	7.45	1.86	1×10^{-3}	7.36	2.91	5.14	1×10^{-3}
$11^{\triangle}$	-50.9	31.7	4.38	14.69	16.62	3×10^{-3}	3.40	1.45	5.70	2×10^{-3}
$12^{\otimes}$	-31.6	15.9	1.65	2.38	3.06	1×10^{-3}	5.49	3.79	6.28	3×10^{-3}
$13^{\bullet}$	-35.2	4.4	5.03	4.52	3.07	1×10^{-3}	9.59	3.86	11.67	3×10^{-3}
$14^{\star}$	-57.3	19.9	7.30	4.51	1.78	1×10^{-3}	5.71	1.48	12.17	2×10^{-3}
$15^{\dagger}$	-74.8	27.7	1.24	5.27	5.36	2×10^{-3}	2.25	3.24	15.68	1×10^{-3}

model parameters is sufficient, thanks to symmetry. Therefore, it is possible to obtain a faster solution.

5.2. Experimental Results and Discussion

The optimized modification matrix parameters are presented in Appendix B. If these parameters are closer to zero, less modification is required, and our initial guess is accurate. As described in Eq. 63, the loading conditions from the mobile platform frame have zero components for z-axis force and moment. It means 3rd and 6th columns of the inverse of the stiffness matrix $\boldsymbol{K}'_C$ are multiplied with zero values during optimization of the modification matrix. This introduces redundancy in optimizing the modification matrix; hence, this set of parameters is not unique. Furthermore, this redundancy fits the model to the experimental data as if it is reserved for fine adjustment. In this regard, the computed modification matrix is a solution of a Pareto-front optimal set.

Table 3 presents the average root-mean-square (RMS) of the errors between the model and experimental data with updated and non-updated stiffness matrix parameters for all loads. The effectiveness of parameter update can be easily seen by comparing the $F_y/\Delta y$ load/deflection relation at 25 kg of mass loading condition for updated and non-updated results. A reduction from 879.5 µm RMS error to 5.9 µm RMS error is achieved. The error set of $F_y/\Delta y$ shows the best performance enhancement and has the minimum error set after the parameter update, even though other loads/deflection sets have lower errors before the parameter update. The reason for this behavior lies

in the definition of the objective function in Eq. 64. Since the large loads and large deflections are related to the stiffness parameters, a slight modification in these parameters is amplified by the large load/deflection relation, which results in a greater error achieved from the model. Therefore, the optimization algorithm prioritizes reducing the large deflection errors by adjusting their related stiffness parameters. It can be said that large load/deflection relation defines a weight on the objective function. As a result, small load/deflection relations become less critical. It can be proved by comparing $F_y/\Delta z$ RMS errors before and after the parameter updates. The error remains the same because $F_y/\Delta z$ has the minimum load/deflection values as shown in Table 3.

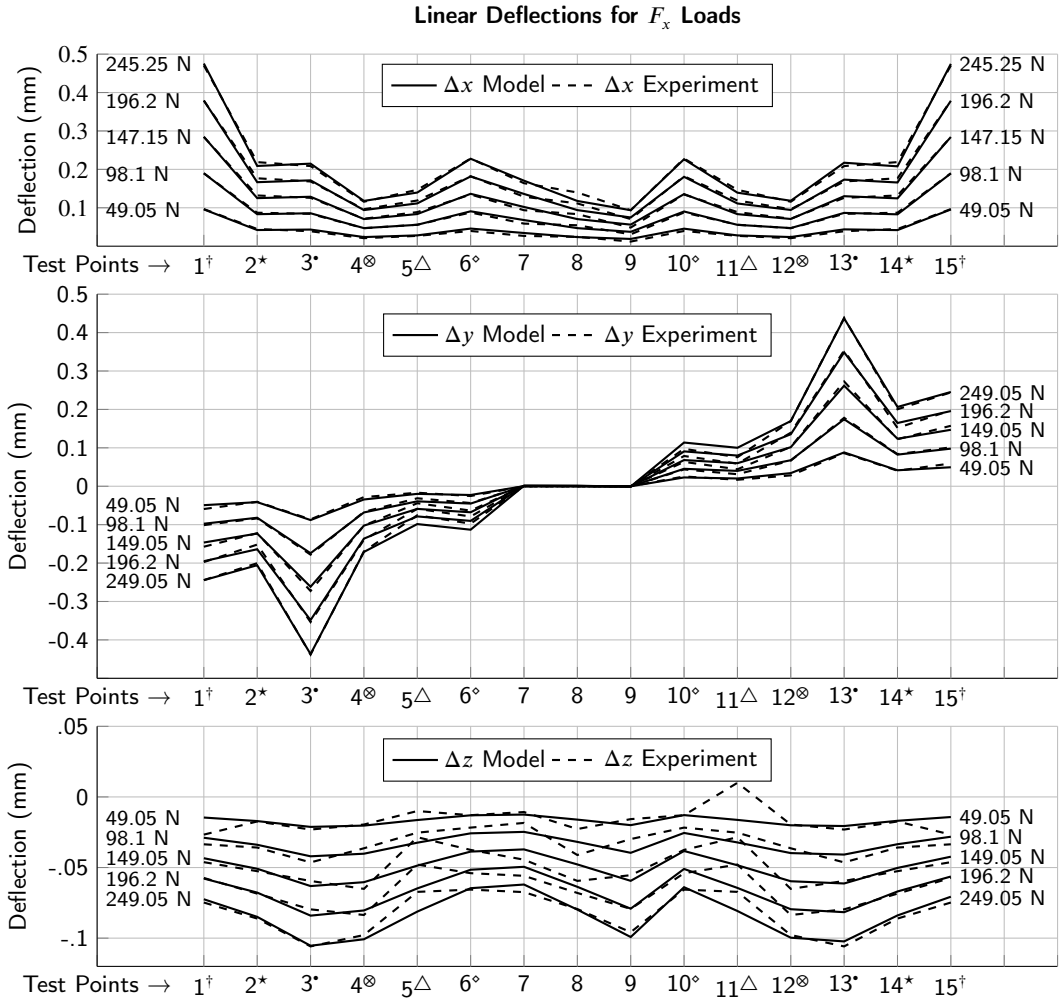

Figure 11: Linear deflections for loads along F_x.

Table 4 shows absolute deflection errors between the model and the experimental data. The presented results are the average errors considering all loading conditions from 49.05 N to 245.25 N at each test point. The same upper index symbol indicates symmetric test points. x-axis deflections for F_x load and y-axis deflections for F_y load show smaller average error than 10 μm, but only in one occurrence for $F_x/\Delta x$ load/deflection relation at test point 8 the error surpasses 10 μm. $F_x/\Delta y$ and $F_y/\Delta x$ load/deflection relations also present a smaller error performance than 10 μm except at three occurrences at test points 5, 11, and 6.

In Fig. 11, 12, and 13, measured deflections and the model's output, which is updated by the modification matrix, are illustrated. When the obtained model is compared with the experimental data, a good overlap is observed even for large deflection values. If the joint clearances were more significant than anticipated or the internal stresses were higher than predicted, the stiffness problem would take on a much more non-linear mathematical nature. In this case,

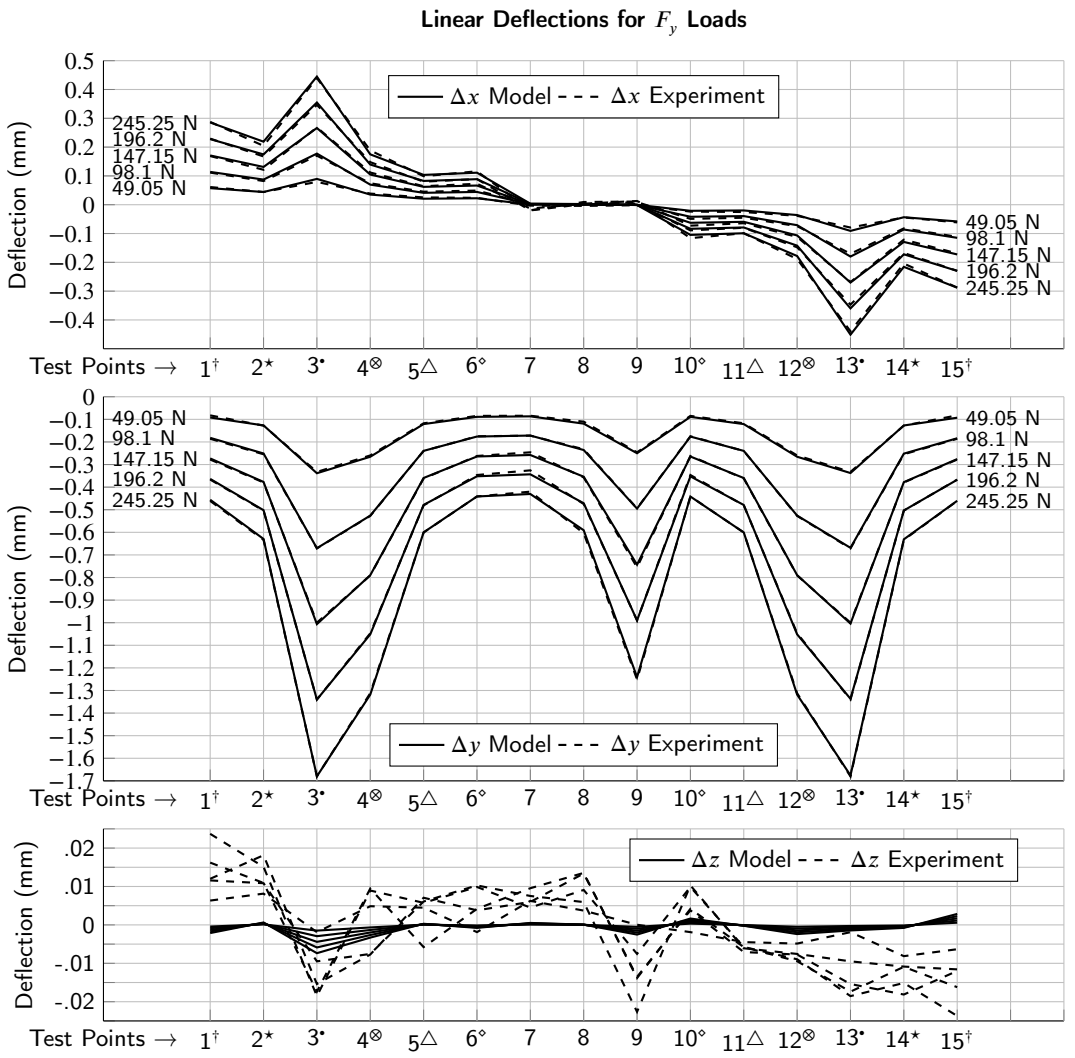

Figure 12: Linear deflections for loads along F_y.

the obtained model and the designed parameters would be insufficient to solve the problem. After its parameters are updated correctly, we conclude that the stiffness model captures the manipulator's general characteristics. In Fig. 11 and 12, x-axis deflections for F_x load and y-axis deflections for F_y load display the greatest deflection values. 0.5 mm and 1.7 mm maximum deflections are recorded for $F_x/\Delta x$ and $F_y/\Delta y$ load/deflection relations, respectively. Since there is no force component along z-axis, minimal deflection values are recorded along this axis. When the model's performance for angular deflections is examined, it provides a good match for the angular deflections about y- and x-axes. Maximum angular deflections are smaller than 1.6° for y-axis rotation under F_x load and 1° for x-axis rotation under F_y load.

In this part, a model fitting process was applied to the existing stiffness model from the previous section. It is possible to update the model considering the height difference between the distal and proximal parallelograms. In that case, distal parallelograms would experience only forces since their links are at the same height level with the mobile platform. However, the proximal parallelograms would experience both force and moment due to the height difference. This moment can be computed considering the load distribution in the joint space. This computation is explained in Eq. 63. This modified force and moment vector is computed using the virtual moment arm parameters obtained during the model fitting process to comply with the experiment results.

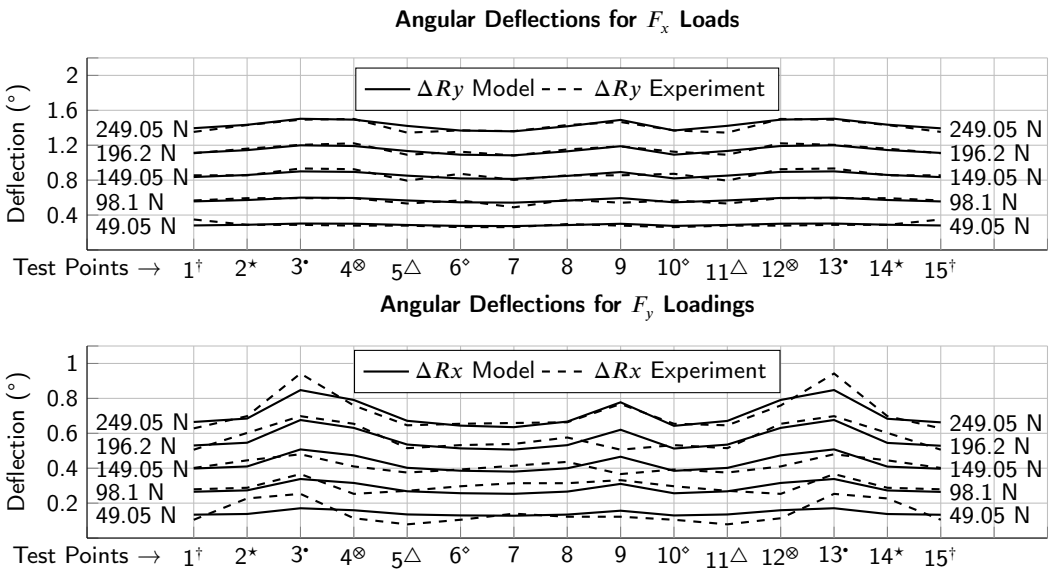

Figure 13: Angular deflections about x- and y- axes.

6. Conclusion and Discussion

This paper uses a case study to present stiffness model acquisition via the virtual joint method (VJM) of parallel manipulators with serially connected sub-loops in their limbs. Auxiliary force effects on the end-effector's compliant deflection are considered via the superposition principle. In order to investigate the performance of the auxiliary force consideration method, two VJM models of the manipulator are acquired in which one is only subjected to forces at the end-effector, and the other one is subjected to auxiliary forces and end-effector forces. Auxiliary forces are calculated to be one-tenth of the end-effector forces; hence, minimal differences between the two models are expected. The outputs are compared with a finite element model subjected to auxiliary and end-effector forces. Nine test points are determined within the manipulator's workspace, and compliant deflections are obtained for each x- and y-axes in the simulation environment. 18 simulation test results are obtained with the proposed methodology. Among these results, (1) in 8 tests, the proposed method produced better results compared to the case where only the forces at the end-effector are considered, (2) in 6 tests, both methods produced the same results and (3) in 4 tests, the proposed method produced relatively worse results. The proposed method (VJM_{EAB}) may output better results if an iterative method is adopted. Nevertheless, both VJM models have captured the configuration-dependent stiffness characteristics of the manipulator. Hence, it can be concluded that the proposed VJM model acquisition procedure for parallel manipulators that have serially connected sub-loops is applicable. Also, we conclude that the proposed superposition methodology works when considering the auxiliary forces; however, this feature calls for further investigation. In addition, the 6-DoF VJM model runs at 10 kHz in a Matlab environment and can even run faster if the size of the stiffness matrix is made smaller by discarding the columns and rows of unneeded deflection axes.

The VJM model accuracy and performance are also compared with the experimental results obtained from the actual manipulator. 49.05 N to 245.25 N loads are applied to the real manipulator along x- and y-axes, and compliant deflection results are obtained. Next, a modification matrix is proposed to update the VJM model parameters using experimental data. It was able to capture configuration-dependent and configuration-independent gain values for enhancing the accuracy of the stiffness model. Then, the VJM model output is compared with the experiment results. The maximum average RMS error of 879.5 μm is reduced to 5.9 μm. Hence, the ability of the proposed VJM method to represent the configuration-dependent stiffness behavior of the manipulator is experimentally verified. This proves the soundness of our proposed stiffness modeling solution of having serially connected sub-loops at the limbs of parallel manipulators and the vitality of the modification matrix for the stiffness parameter update process.

Acknowledgements

The study is supported in part by The Scientific and Technological Research Council of Turkey via grant number 116M272. We thank Dr. Emre Uzunoğlu, Ms. Merve Özkahya, and Mr. Erkan Paksoy, for contribution to the design of the experimental test setup.

References

[1] T. Huang, X. Zhao, D. J. Whitehouse, Stiffness estimation of a tripod-based parallel kinematic machine, IEEE Transactions on Robotics and Automation 18 (2002) 50–58.
[2] A. Ghali, A. Neville, T. G. Brown, Structural Analysis: A Unified Classical and Matrix Approach, CRC Press, 2014.
[3] A. Klimchik, D. Chablat, A. Pashkevich, Stiffness modeling for perfect and non-perfect parallel manipulators under internal and external loadings, Mechanism and Machine Theory 79 (2014) 1–28.
[4] A. Pashkevich, D. Chablat, P. Wenger, Stiffness analysis of overconstrained parallel manipulators, Mechanism and Machine Theory 44 (2009) 966–982.
[5] J. K. Salisbury, J. J. Craig, Articulated hands: Force control and kinematic issues, The International Journal of Robotics Research 1 (1982) 4–17.
[6] C. Gosselin, Stiffness mapping for parallel manipulators, IEEE Transactions on Robotics and Automation 6 (1990) 377–382.
[7] C. Gosselin, Stiffness analysis of parallel mechanisms using a lumped model, International Journal of Robotics and Automation. 17 (2002) 17–27.
[8] G. Wu, S. Bai, J. Kepler, Mobile platform center shift in spherical parallel manipulators with flexible limbs, Mechanism and Machine Theory 75 (2014) 12–26.
[9] A. G. Hoevenaars, P. Lambert, J. L. Herder, Jacobian-based stiffness analysis method for parallel manipulators with non-redundant legs, Proceedings of the Institution of Mechanical Engineers, Part C: Journal of Mechanical Engineering Science 230 (2016) 341–352.
[10] İ. Görgülü, G. Carbone, M. İ. C. Dede, Time efficient stiffness model computation for a parallel haptic mechanism via the virtual joint method, Mechanism and Machine Theory 143 (2020) 103614.
[11] C. Yang, Q. Chen, J. Tong, Q. Li, Elastostatic stiffness analysis of a 2 p ur-p sr overconstrained parallel mechanism, International Journal of Precision Engineering and Manufacturing 20 (2019) 569–581.
[12] C. Yang, Q. Li, Q. Chen, L. Xu, Elastostatic stiffness modeling of overconstrained parallel manipulators, Mechanism and Machine Theory 122 (2018) 58–74.
[13] A. Klimchik, A. Pashkevich, D. Chablat, Fundamentals of manipulator stiffness modeling using matrix structural analysis, Mechanism and Machine Theory 133 (2019) 365–394.
[14] A. Pashkevich, A. Klimchik, D. Chablat, Enhanced stiffness modeling of manipulators with passive joints, Mechanism and Machine Theory 46 (2011) 662–679.
[15] A. Klimchik, A. Pashkevich, D. Chablat, G. Hovland, Compliance error compensation technique for parallel robots composed of non-perfect serial chains, Robotics and Computer-Integrated Manufacturing 29 (2013) 385–393.
[16] J.-P. Merlet, Parallel robots, volume 128, Springer Science and Business Media, 2006.
[17] S. Briot, I. A. Bonev, Are parallel robots more accurate than serial robots?, Transactions of the Canadian Society for Mechanical Engineering 31 (2007) 445–455.
[18] L. Romdhane, Z. Affi, M. Fayet, Design and singularity analysis of a 3-translational-dof in-parallel manipulator, Journal of Mechanical Design 124 (2002) 419–426.
[19] K. H. Harib, K. A. Moustafa, A. S. Ullah, S. Zenieh, Parallel, Serial and Hybrid Machine Tools and Robotics Structures: Comparative Study on Optimum Kinematic Designs, IntechOpen, 2012.
[20] G. Kiper, M. İ. C. Dede, E. Uzunoğlu, E. Mastar, Use of hidden robot concept for calibration of an over-constrained mechanism, in: 14th International Federation for the Promotion of Mechanism and Machine Science World Congress, volume 5, IFToMM, 2015, pp. 2822–2826.
[21] B. Hu, Z. Huang, Kinetostatic model of overconstrained lower mobility parallel manipulators, Nonlinear Dynamics 86 (2016) 309–322.
[22] R. Vertechy, V. Parenti-Castelli, Static and stiffness analyses of a class of over-constrained parallel manipulators with legs of type us and ups, in: Proceedings 2007 IEEE International Conference on Robotics and Automation, IEEE, 2007, pp. 561–567.
[23] J. Ding, C. Wang, H. Wu, Accuracy analysis of redundantly actuated and overconstrained parallel mechanisms with actuation errors, Journal of Mechanisms and Robotics 10 (2018). 061010.
[24] W.-a. Cao, H. Ding, D. Yang, A method for compliance modeling of five degree-of-freedom overconstrained parallel robotic mechanisms with 3T2R output motion, Journal of Mechanisms and Robotics 9 (2017). 011011.
[25] W.-a. Cao, H. Ding, A method for stiffness modeling of 3R2T overconstrained parallel robotic mechanisms based on screw theory and strain energy, Precision Engineering 51 (2018) 10–29.
[26] W.-a. Cao, H. Ding, W. Zhu, Stiffness modeling of overconstrained parallel mechanisms under considering gravity and external payloads, Mechanism and Machine Theory 135 (2019) 1–16.
[27] T. Sun, B. Lian, Y. Song, Stiffness analysis of a 2-dof over-constrained rpm with an articulated traveling platform, Mechanism and Machine Theory 96 (2016) 165–178.
[28] A. Cammarata, Unified formulation for the stiffness analysis of spatial mechanisms, Mechanism and Machine Theory 105 (2016) 272–284.
[29] A. Klimchik, A. Pashkevich, D. Chablat, Stiffness modeling of navaro ii transmission system, IFAC-PapersOnLine 52 (2019) 701–706.
[30] E. Paksoy, M. I. C. Dede, G. Kiper, Experimental compliance matrix derivation for enhancing trajectory tracking of a 2-dof high-accelerated over-constrained mechanism, in: IFToMM Asian conference on Mechanism and Machine Science, Springer, 2021, pp. 354–362.

Appendix A

Table A1

Finite Element Analysis (FEA) and Virtual Joint Method (VJM). The compliant deflection unit is μm. Sub-indices E, A, and B indicate the force is applied from the frames $\mathcal{F}(E)$, $\mathcal{F}(A)$, and $\mathcal{F}(B)$.

	Test Point 1						Test Point 2						Test Point 3					
	FEA_{EAB}		VJM_{E}		VJM_{EAB}		FEA_{EAB}		VJM_{E}		VJM_{EAB}		FEA_{EAB}		VJM_{E}		VJM_{EAB}	
Force Direction	x	y	x	y	x	y	x	y	x	y	x	y	x	y	x	y	x	y
0°	1.7	0	1.7	0	1.9	0	2.6	0	2.5	0	2.9	0	4.4	0	4.3	0	4.9	0
30°	1.5	33.4	1.4	33.5	1.7	33.5	2.2	16.7	2.2	16.8	2.5	16.8	3.8	11.8	3.7	11.8	4.3	11.8
60°	0.8	57.9	0.8	58.1	1	58.1	1.3	29	1.2	29.1	1.4	29.1	2.2	20.5	2.1	20.5	2.5	20.5
90°	0	66.9	0	67.1	0	67.1	0	33.5	0	33.5	0	33.5	0	23.6	0	23.7	0	23.7
120°	-0.9	58	-0.8	58.1	-1	58.1	-1.3	29	-1.2	29.1	-1.4	29.1	-2.2	20.5	-2.1	20.5	-2.5	20.5
150°	-1.5	33.5	-1.4	33.5	-1.7	33.5	-2.3	16.7	-2.1	16.8	-2.5	16.8	-3.9	11.8	-3.7	11.8	-4.3	11.8

	Test Point 4						Test Point 5						Test Point 6					
	FEA_{EAB}		VJM_{E}		VJM_{EAB}		FEA_{EAB}		VJM_{E}		VJM_{EAB}		FEA_{EAB}		VJM_{E}		VJM_{EAB}	
Force Direction	x	y	x	y	x	y	x	y	x	y	x	y	x	y	x	y	x	y
0°	16.9	-16.3	17.8	-17.7	17.4	-16.4	5.7	-9.9	5.8	-10.5	6	-9.9	3.9	-12.6	3.9	-12.9	4.1	-12.6
30°	5.83	-1.44	6.6	-2.6	6.2	-1.4	-0.3	8.6	-0.2	8.2	0	8.6	-3.1	26.5	-3.1	26.3	-2.9	26.6
60°	-6.84	13.9	-6.4	13.2	-6.6	13.9	-6.2	24.8	-6.2	24.6	-6.1	24.9	-9.2	58.5	-9.2	58.5	-9.1	58.6
90°	-17.7	25.5	-17.7	25.5	-17.7	25.5	-10.5	34.4	-10.5	34.5	-10.5	34.5	-12.9	74.8	-12.9	75	-12.9	75
120°	-23.9	30.3	-24.3	31	-24.1	30.3	-12	34.8	-12	35.1	-12.1	34.8	-13.1	71.1	-13.1	71.4	-13.2	71.2
150°	-23.6	27	-24.3	28.1	-23.9	27	-10.2	25.8	-10.3	26.3	-10.5	25.8	-9.8	48.3	-9.8	48.7	-10	48.4

	Test Point 7						Test Point 8						Test Point 9					
	FEA_{EAB}		VJM_{E}		VJM_{EAB}		FEA_{EAB}		VJM_{E}		VJM_{EAB}		FEA_{EAB}		VJM_{E}		VJM_{EAB}	
Force Direction	x	y	x	y	x	y	x	y	x	y	x	y	x	y	x	y	x	y
0°	11.6	-29.6	11.8	-30.2	11.8	-29.7	16.1	-21.4	16.7	-22.5	16.4	-21.4	97.6	-48.1	101.9	-50.5	96.7	-47.6
30°	-5	19.5	-4.9	19.1	-4.9	19.6	2.7	0	3.2	-1	2.9	0	59.3	-27.4	63.1	-29.6	58.3	-26.8
60°	-20.3	63.4	-20.3	63.3	-20.2	63.6	-11.4	21.3	-11.1	20.8	-11.3	21.4	4.7	0.7	7.2	-0.6	4.3	1.1
90°	-30.2	90.3	-30.2	90.5	-30.2	90.5	-22.5	37	-22.5	37.1	-22.5	37	-52.5	29.1	-51.1	28.9	-50.9	28.7
120°	-32	93	-32	93.5	-32.1	93.2	-27.6	42.7	-27.9	43.4	-27.7	42.8	-96.8	50.1	-96.1	50.7	-92.4	48.7
150°	-25.2	70.8	-25.3	71.4	-25.3	70.9	-25.2	37	-25.8	38	-25.5	37.1	-115.3	57.8	-115.2	59	-109.2	55.6

Appendix B

Table B1

Optimized modification matrix and virtual moment arms parameters. (N·m/m and N/rad units are simplified to N.)

k_1	−682581.69 N/m	k_{18}	−9860.23 N	k_{35}	−133839.70 N	k_{52}	−12712.36 N·m/rad
k_2	−176694.31 N/m	k_{19}	445958.51 N	k_{36}	455.36 N·m/rad	k_{53}	−1229.68 N·m/rad
k_3	6931081.96 N/m	k_{20}	36396.56 N	k_{37}	297044.99 N	k_{54}	1353507.83 N/m
k_4	305814.59 N·m/rad	k_{21}	448089.83 N	k_{38}	−6789.15 N	k_{55}	110128.52 N
k_5	319756.95 N·m/rad	k_{22}	−2013299.99 N/m	k_{39}	−472.10 N	k_{56}	1181559.95 N
k_6	−614.58 N·m/rad	k_{23}	−6392.84 N/m	k_{40}	−412917.17 N	k_{57}	−27232.35 N·m/rad
k_7	−585347.64 N/m	k_{24}	1166028.11 N/m	k_{41}	−192.70 N	k_{58}	−10081.42 N
k_8	−538600.05 N/m	k_{25}	271346.39 N·m/rad	k_{42}	−10199.16 N	k_{59}	−19382.79 N
k_9	−38045.02 N	k_{26}	367542.60 N·m/rad	k_{43}	−62556.25 N/m	k_{60}	2427.17 N
k_{10}	−172485.58 N·m/rad	k_{27}	−62.95 N·m/rad	k_{44}	−28711.40 N/m	k_{61}	−12128.66 N
k_{11}	5288.43 N·m/rad	k_{28}	−23459.22 N/m	k_{45}	48277184.32 N/m	k_{62}	−36977.22 N
k_{12}	−2463245.79 N/m	k_{29}	−16845.07 N/m	k_{46}	262364.31 N·m/rad	k_{63}	1214.03 N
k_{13}	−19527.29 N	k_{30}	89855.32 N	k_{47}	401376.50 N·m/rad	h_1	7.68 m
k_{14}	2021068.50 N	k_{31}	167530.02 N·m/rad	k_{48}	308.36 N·m/rad	h_2	3.54 m
k_{15}	1114.64 N·m/rad	k_{32}	605.51 N·m/rad	k_{49}	−2332.49 N/m		
k_{16}	326089.54 N	k_{33}	857749.02 N/m	k_{50}	−253469.03 N/m		
k_{17}	57396.59 N	k_{34}	−8392.46 N	k_{51}	−161419.91 N		